Quaternary magnetic and oxygen isotope stratigraphy in diatom-rich sediments of the southern Gardar Drift (IODP Site U1304, North Atlantic)

Chuang Xuan [1], James E.T. Channell [2], David A. Hodell [3]

1. School of Ocean and Earth Science, National Oceanography Centre Southampton, University of Southampton, Waterfront Campus, European Way, Southampton SO14 3ZH, UK
2. Department of Geological Sciences, University of Florida, 241 Williamson Hall, POB 112120, Gainesville, FL 32611, USA
3. Godwin Laboratory for Palaeoclimate Research, Department of Earth Sciences, Downing Street, Cambridge CB2 3EQ, UK

Abstract

The sediment sequence from Integrated Ocean Drilling Program (IODP) Site U1304 (53°03.40′N, 33°31.78′W; water depth, 3024 m) on the southern Gardar Drift, North Atlantic Ocean, covers the last ~1.8 Myr with a mean sedimentation rate of ~15 cm/kyr. At Site U1304, paleomagnetic directional and relative paleointensity (RPI) records have been generated for the last ~1.5 Myr, and benthic oxygen isotope data for the last ~1 Myr. The age model for Site U1304 was established by matching $\delta^{18}O$ and RPI data to calibrated reference records. Prominent intervals of diatom mats at Site U1304 are associated with the latter stages of interglacial marine isotope stages (MIS) 9, 11, 13, 15, 21, 27 and 35, and with the weak glacial of MIS 14. The deposition of diatom mats, and associated diluted magnetic mineral concentrations, leads to weak magnetizations and

susceptibilities in these intervals. Comparison of histograms of paleomagnetic directions and RPI from diatom-rich sediments and from surrounding silty clays indicates that, although results from diatom-rich sediments are more scattered, the occurrence of diatom mats does not appreciably distort the paleomagnetic directional and RPI records. Site U1304 sediments record the Matuyama/Brunhes boundary (~772 ka), the Jaramillo Subchron (~993-1071 ka) and the Cobb Mountain Subchron (~1193-1219 ka), as well as three apparent geomagnetic excursions in the Matuyama Chron, interpreted as the "Kamikatsura/Santa Rosa", "Punaruu", and "Gardar" excursions, at ~888 ka, ~1124 ka, and ~1463 ka, respectively. The Site U1304 RPI record can be correlated with the PISO-1500 RPI stack and with other high-resolution RPI records from the North Atlantic Ocean. Wavelet analyses performed on the Site U1304 RPI record and a new high-resolution North Atlantic paleointensity stack for the last 1500 kyr (HINAPIS-1500), comprising Ocean Drilling Program (ODP) Sites 983, 984 and IODP Sites U1306 and U1304, did not reveal significant orbital power.

Keywords: Quaternary; North Atlantic; Relative Paleointensity; Magnetic Excursions; Oxygen Isotopes; Diatoms; IODP Site U1304

1. Introduction

Site U1304 (53°03.40′N, 33°31.78′W; water depth, 3024 m) was drilled in October 2004 from the R/V *JOIDES Resolution* during Integrated Ocean Drilling Program (IODP) Expedition 303. The objective was to obtain a high-resolution environmental record of the last few million years (Myrs) within the central Atlantic ice-rafted debris (IRD) belt,

48 at a water depth sufficient to monitor past North Atlantic Deep Water (Expedition 303
49 Scientists, 2006). The site lies in a semi-enclosed basin at the southern end of the Gardar
50 Drift, to the north of the Charlie Gibbs Fracture Zone (Figure 1). Four holes (U1304A,
51 U1304B, U1304C, and U1304D) were cored at Site U1304 to obtain an apparently
52 continuous ~270-m composite sediment sequence covering the last ~1.8 Myrs. With an
53 average sedimentation rate of ~15 cm/kyr for the ~270-m stratigraphic section, Site
54 U1304 represents one of the higher resolution Quaternary deep-sea sediment archives
55 available from the North Atlantic Ocean, although sedimentation rates are highly variable
56 (~5 to >40 cm/kyr) due to fluctuating biogenic (mainly diatom) abundance.
57
58 Sediments at Site U1304 consist of inter-bedded, gray-green calcareous nannofossil and
59 diatomaceous oozes with clay and silty clay (Expedition 303 Scientists, 2006). The
60 elevated sedimentation rates at Site U1304 are attributable to the remarkable and unusual
61 occurrence of laminated and massive diatom mats on scales of a few centimeters to tens
62 of meters. The diatomaceous ooze deposition comprises mainly the planktic, araphid,
63 needle-like species *Thalassiothrix longissima*. The diatom-rich intervals are episodic and
64 discontinuous, but are present throughout the entire recovered section back to ~1.8 Ma
65 (Expedition 303 Scientists, 2006; Shimada et al., 2008; Romero et al., 2011). The only
66 analogous documented occurrence of diatom mats in the North Atlantic Ocean is during
67 the last interglacial, marine isotope stage (MIS) 5, in conventional piston Core EW9303-
68 17 (57°N, 37°W; water depth 3233 m), located ~500 km NW of Site U1304 (Figure 1).
69 The occurrence of diatom mats in MIS 5 of Core EW9303-17 was attributed by Bodén
70 and Backman (1996) to its proximity to the Sub-arctic Convergence (SAC), which is a

71 distinct oceanic front between the warm and saline North Atlantic Current and the
72 Irminger Current, and the cold and less saline East Greenland Current and the waters that
73 flow out of the Labrador Sea (Ruddiman and Glover, 1975). Shimada et al. (2008), based
74 on principal component analysis of the diatom assemblage, concluded that the switching
75 between warm- and cold-water diatom assemblages occurred concurrently with diatom
76 mat deposition, which implies that diatom mat deposition was related to migrations of the
77 SAC over the site, analogous to the interpretation of Bodén and Backman (1996). Diatom
78 occurrence at Site U1304 is not simply related to glacial-interglacial cycles (Shimada et
79 al., 2008) and, during the last interglacial, productivity apparently peaked at the MIS
80 5d/5e boundary (Romero et al., 2011). According to Romero et al. (2011), surface waters
81 alone would not have provided the necessary nutrients to sustain the observed diatom
82 productivity at Site U1304. The unique occurrence of diatom mats throughout the
83 Quaternary section at Site U1304 implies episodic incursion of silicate- and nitrate-rich
84 Sub-Antarctic Mode Water (SAMW), as a result of slow-down of Iceland-Scotland
85 Overflow Water (ISOW), and sporadic convective mixing of the water column (Romero
86 et al., 2011).
87
88 During the last few decades, accumulation of relative paleointensity (RPI) data from
89 deep-sea sediments and the construction of RPI stacks (e.g. Guyodo and Valet, 1999;
90 Stoner et al., 2002; Laj et al., 2004; Valet et al., 2005; Channell et al., 2009), as well as
91 the documentation of brief geomagnetic excursions (e.g. Laj and Channell, 2007;
92 Roberts, 2008), have added new information pertaining to the geodynamo, and offer
93 potential for high-resolution stratigraphic correlation within polarity chrons. Sedimentary

RPI records covering the last ~1.5 Myr with mean sedimentation rates above 10 cm/kyr are rare, and include Ocean Drilling Program (ODP) Sites 983 and 984 (Channell et al., 1997, 2002; Channell, 1999; Channell and Kleiven, 2000) and IODP Site U1306 (Channell et al., 2014). In this paper, we report high-resolution (mean sedimentation rate ~15 cm/kyr) Quaternary paleomagnetic directional and RPI records for the last ~1.5 Myr, and benthic oxygen isotope ($\delta^{18}O$) data for the last ~1 Myr, from diatom-rich deep-sea sediments recovered at IODP Site U1304 (Figure 1). In view of the variable lithology and sedimentation rates at Site U1304, the site provides a rigorous test of the use of RPI records in stratigraphic correlation.

2. Samples and Methods

2.1 Magnetic measurements

U-channels are samples enclosed in plastic containers with an internal ~1.8×1.9 cm^2 cross-section and the same length as the core sections (usually 150 cm), with a clip-on plastic lid that constitutes one of the sides that seals the samples to minimize dehydration (Tauxe et al., 1983; Weeks et al., 1993; Nagy and Valet, 1993). U-channel samples were collected from the archive halves of core sections within the composite splice derived from Holes U1304A, U1304B, and U1304D (Table T21 in Expedition 303 Scientists, 2006), except for occasional intervals (i.e. 74.76-77.76 m composite depth (mcd), and 177.74-182.18 mcd) where sampling switched to core sections not on the composite splice, because the splice in these intervals was found to be affected by coring disturbance. Our u-channel sampling covered the 0-225 mcd interval, except for a ~3.5-m gap in the 197.9-201.4 mcd interval where a thick diatom mat was impossible to sample

without extensive sediment disturbance. Compared with the shipboard data acquired using split half-core sections, u-channel measurements have a number of advantages: (1) u-channels are taken from the center of the split core to avoid disturbed core margins; (2) complete stepwise alternating field (AF) demagnetization can be carried out to define magnetization components; (3) the smaller diameter sample access and the narrower response function of the u-channel magnetometer introduce less convolution/smoothing of sequential measurements; (4) u-channel measurements are made at higher spatial resolution (typically 1-cm spacing) than shipboard measurements (typically 5-cm; Weeks et al., 1993); and (5) laboratory-induced magnetizations can be measured to develop RPI proxies.

Remanent magnetization measurements for Site U1304 u-channel samples were carried out on a 2G Enterprises pass-through superconducting rock magnetometer (SRM) designed to measure u-channel samples at the University of Florida. Measurements for each u-channel were made at 1-cm intervals with a 10-cm "leader" interval and a 10-cm "trailer" interval, immediately before/after the ends of the sample reached/passed the center of the magnetometer sensor region. The "leader" and "trailer" measurements serve the dual functions of monitoring the background magnetic moment and allowing for future signal deconvolution. The natural remanent magnetization (NRM) of u-channel samples was measured before demagnetization, and then after progressive AF demagnetization at peak fields of 20-60 mT in 5 mT increments, 60 to 80 mT in 10 mT increments, and at 100 mT (12 steps in total). For each 1-cm interval, characteristic remanent magnetization (ChRM) directions were calculated using the principal

140 component analysis (PCA, Kirschvink, 1980) and the UPmag software (Xuan and
141 Channell, 2010). PCA calculations used NRM data acquired during the 20-80 mT
142 demagnetization interval without anchoring directions to the origin of orthogonal
143 projections, and is associated with maximum angular deviation (MAD) values that
144 monitor the quality of the ChRM directions.
145
146 After completion of NRM measurements for each u-channel sample, volume magnetic
147 susceptibility (κ) measurements were made at 1-cm interval resolution using a
148 susceptibility bridge designed for u-channel samples. The susceptibility bridge is
149 equipped with a square-shaped (~3×3 cm^2 cross-section) Sapphire Instruments loop
150 sensor to maximize measurement resolution (Thomas et al., 2003). An anhysteretic
151 remanent magnetization (ARM) was then imparted in a 100-mT peak AF and a 50-μT
152 direct current (DC) bias field, which were both oriented along the long-axis of the u-
153 channel sample. The acquired ARM was measured prior to demagnetization and after
154 stepwise AF demagnetization using the same peak fields used for NRM in the 20-60 mT
155 range. Partial ARMs were then measured during acquisition as the peak AF was
156 increased in 5 mT increments in the 20–60 mT peak field range, in a constant 50-μT DC
157 bias field. After ARM demagnetization and acquisition experiments, an isothermal
158 remanent magnetization (IRM) was acquired for each u-channel sample in a 300-mT DC
159 field, followed by measurements before and after AF demagnetization with the same
160 peak fields applied to the NRM in the 20-60 mT range. IRMs were also acquired in a
161 950-mT DC field followed by measurement without demagnetization. Subsequently, an
162 IRM was acquired in a 300-mT DC back-field, opposite to that for the 950-mT IRM, and

163 measured. The IRM acquired in a 950-mT DC field and in a subsequent 300-mT back-
164 field was used to calculate the S-ratio (Bloemendal et al., 1992): S-ratio = [(IRM.
165 $_{300mT}$/IRM$_{950mT}$)+1]/2. S-ratios were calculated for each 1-cm measurement interval, and
166 provide information on concentration changes of high coercivity magnetic components.
167
168 NRM intensity, normalized by the intensity of laboratory-induced magnetizations, is
169 often used as a proxy for relative paleointensity (Levi and Banerjee, 1976; King et al.,
170 1983; Tauxe et al., 1993). Normalization is usually carried out using ARM and IRM
171 intensities, or less commonly magnetic susceptibility, to compensate for changes in
172 concentration of remanence carrying grains down-core. Our estimates of RPI proxies for
173 Site U1304 utilize NRM intensity data as well as ARM intensities (both for
174 demagnetization and acquisition) and IRM intensity data from the 20-60 mT
175 demagnetization steps. For each 1-cm interval, RPI proxies were calculated using the
176 slopes of best-fit lines between NRM lost versus ARM lost, NRM lost versus ARM
177 acquired, and NRM lost versus IRM lost (where the slopes of best-fit lines between NRM
178 lost and ARM acquired are multiplied by -1). RPI estimates were determined using the
179 UPmag software (Xuan and Channell, 2009) and each slope calculation was accompanied
180 by a linear correlation coefficient (r-value) that monitors the quality of the line fit.
181
182 Excess sediment collected during u-channel sampling was sealed in plastic bags. One bag
183 of bulk sediment was collected for each u-channel sample. These bulk samples were used
184 for magnetic property measurements on a Princeton Measurements Corporation vibrating
185 sample magnetometer (VSM) at the University of Florida. For each bulk sediment

186 sample, we measured a hysteresis loop and backfield remanence curve to determine ratios
187 of hysteresis parameters: M_r/M_s and H_{cr}/H_c, where M_r is saturation remanence, M_s is
188 saturation magnetization, H_{cr} is coercivity of remanence, and H_c is coercive force.
189
190 *2.2 Diatom mat occurrence*
191 We recorded the occurrence of diatom mats in Site U1304 sediments during sampling by
192 visual inspection of u-channel samples, and from shipboard digital image scans. Diatom-
193 rich sediments have characteristic "oatmeal" texture and often have sharp contacts with
194 inter-bedded silts and clays. For each 1-cm interval of sediment, we assigned a diatom
195 richness value (DRV) of "1" to intervals that comprise predominantly diatom mats. A
196 DRV of "0.5" was assigned to 1-cm intervals that comprise sediment containing
197 disseminated diatoms. For sediment intervals that comprise silts and clays without
198 macroscopic evidence for diatoms, "0" was assigned as the DRV.
199
200 *2.3 Oxygen isotopes*
201 Oxygen isotope ratios ($\delta^{18}O$) measured on the benthic foraminifera *Cibicidoides*
202 *wuellerstorfi* have been reported previously for the 23.6-m long (0 to ~125 ka) piston
203 Core KN166-14-JPC13 (hereafter referred to as JPC-13) from the same location as Site
204 U1304 (Fig. 1, Hodell et al., 2010), and for the 15-25 mcd interval (MIS 5) of Site U1304
205 (Hodell et al., 2009). Oxygen isotope ($\delta^{18}O$) data for the 25-166 mcd interval at Site
206 U1304 were also measured on specimens of *Cibicidoides wuellerstorfi* at ~5-cm
207 stratigraphic resolution. Specimens of *Cibicidoides wuellerstorfi* were selected from the
208 >150 μm size fraction. Isotope measurements at the University of Florida were made

209 using a Finnigan-MAT 252 isotope ratio mass spectrometer coupled with a Kiel III
210 carbonate preparation device, and are reported in standard delta notation relative to
211 Vienna Pee Dee Belemnite (VPDB) using NBS-19 for calibration. The estimated
212 analytical error for $\delta^{18}O$ data is better than ±0.1‰. Subsequently, additional stable
213 isotope analyses were performed on a VG SIRA mass spectrometer at the University of
214 Cambridge with a Multicarb system for samples of >80 μg mass. Analytical precision for
215 the measurements is estimated to be ±0.08‰ for $\delta^{18}O$. For smaller samples (<80 μg)
216 analyzed in Cambridge, measurements were performed on a Thermo Finnigan MAT253
217 mass spectrometer fitted with a Kiel IV carbonate device. Analytical precision for these
218 samples is estimated to be ±0.08‰ for $\delta^{18}O$. No offset in $\delta^{18}O$ were observed among the
219 various instruments employed in Florida and Cambridge.
220
221 **3. Age Model**
222 The age model was constructed for the top ~225 mcd of Site U1304 by correlating
223 volume susceptibility (κ), $\delta^{18}O$, and the RPI proxy, to reference records. For the top ~22
224 mcd, susceptibility data from Site U1304 were correlated to those from Core JPC-13
225 from the same location (Figure 1). The chronology for the 0-80 ka interval of JPC-13
226 (Hodell et al., 2010) was based on correlation of millennial scale features in the benthic
227 $\delta^{18}O$ record of JPC-13 to that of Core MD95-2042 from the Portuguese Margin, which
228 was synchronized with Greenland and Antarctic ice cores (Shackleton et al., 2004). Ages
229 for the 80-125 ka interval of JPC-13 were based on correlation of benthic $\delta^{18}O$ data of
230 JPC-13 to the LR04 benthic $\delta^{18}O$ stack (Lisiecki and Raymo, 2005). An unambiguous
231 correlation between the susceptibility records of Site U1304 and JPC-13 was established

232 using 19 tie points (Table 1) to transfer the age model of JPC-13 to Site U1304 for the
233 last ~125 kyr (Figure 2a, b). The resulting chronology results in a convincing match
234 (Figure 2c) of the JPC-13 RPI record (Evans, 2006) to the Site U1304 RPI record
235 (estimated using the slopes of best-fit lines of NRM lost versus ARM acquired). For the
236 ~22-166 mcd interval, benthic $\delta^{18}O$ data for the last interglacial at Site U1304 (Hodell et
237 al., 2009) were combined with newer Site U1304 $\delta^{18}O$ data (Figure 3b), and were
238 correlated to the LR04 stack (Lisiecki and Raymo, 2005) to construct a chronology for
239 Site U1304 that extends to ~1 Ma (Figure 2a). Beyond ~1 Ma, we correlated the Site
240 U1304 RPI record, estimated based on slopes of best-fit lines between NRM lost and
241 ARM acquired, to the PISO-1500 RPI stack, which was constructed by tandem matching
242 and stacking of 13 paired RPI and $\delta^{18}O$ records from worldwide locations (Channell et
243 al., 2009). The RPI correlation of Site U1304 to PISO-1500 was achieved using the
244 automated matching algorithm (Match) developed by Lisiecki and Lisiecki (2002). The
245 Site U1304 and the PISO-1500 RPI records were normalized to have zero mean and a
246 standard deviation of 1, prior to the "matching". Site U1304 depth-age tie points,
247 acquired using the above protocol, are listed in Table 1 and plotted on Figure 2a.
248 According to the age model, sedimentation rates at Site U1304 varied from ~5 cm/kyr to
249 >40 cm/kyr over the last ~1.5 Myr (Figure 2a).
250
251 **4. Results and Discussion**
252 *4.1 NRM and Geomagnetic Reversals and Excursions*
253 Site U1304 cores from which the u-channel samples were taken are shown in Figure 3a.
254 ChRM declinations and inclinations, with associated MAD values, are plotted versus

255 depth (mcd) in Figures 3c-e together with the benthic $\delta^{18}O$ data (Figure 3b). The MAD
256 values are largely below 1° and have a mean of ~0.8° for samples from the non-diatom-
257 rich sediment intervals (DRV=0). For samples from diatom-rich sediment intervals
258 (DRV=0.5 or 1, vertical gray bars in Figure 3), MAD values are generally below 5° and
259 have a mean of ~1.7°. These generally low MAD values suggest that ChRM directions
260 are well defined in both non-diatom-rich and diatom-rich sediments, although diatom-
261 rich sediment intervals appear to yield generally noisier ChRM directions (larger MAD
262 values). Representative demagnetization behaviors for non-diatom-rich and diatom-rich
263 sediment intervals are depicted in the top two rows of Figure 4. AF demagnetization
264 using a maximum peak field of 100 mT typically reduced initial NRM intensities of non-
265 diatom intervals to <5% of the initial value. Orthogonal projections of non-diatom-rich
266 sediments (top row in Figure 4) indicate single magnetization components carried by a
267 low-coercivity magnetic mineral. For diatom-rich sediments, occasionally >10% NRM
268 intensity remained after 100 mT peak AF demagnetization (second row in Figure 4),
269 which implies the presence of a high-coercivity remanence carrier. Although NRM data
270 from diatom-rich intervals are apparently more scattered than from the non-diatom
271 intervals, probably due to their lower magnetization intensities, NRM demagnetization
272 data from both diatom-rich and non-diatom intervals still fall largely on a straight line
273 that defines a single magnetization component (Figure 4). Magnetization intensities and
274 susceptibility are usually at least one order of magnitude greater for non-diatom-rich
275 versus diatom–rich intervals (Figures 4 and 5).
276

277 ChRM declinations (light blue points in Figure 3c) were corrected by uniform rotation of
278 each core so that the mean of the corrected declinations (green points in Figure 3c) is
279 oriented north or south for positive and negative inclination intervals, respectively.
280 ChRM inclinations and corrected declinations of Site U1304 can be correlated
281 unambiguously to the geomagnetic polarity time scale (GPTS), to recognize the
282 Matuyama/Brunhes boundary (~138.98 mcd), the Jaramillo Subchron (164.63-176.04
283 mcd), and the Cobb Mountain Subchron (188.17-191.54 mcd) (Figure 3c and d). In
284 addition, three possible magnetic excursions were identified at Site U1304 during the
285 Matuyama Chron at ~149.23-149.34 mcd (Excursion I), ~182.96-183.02 mcd (Excursion
286 II), and ~220.75-221.18 mcd (Excursion III). In Table 2, we list the depths for the
287 polarity reversals and excursions recorded at Site U1304 (including top, bottom, and
288 center mcd) together with their corresponding age estimates according to the age model
289 (Table 1) and the marine isotope stages in which they occur. To identify possible
290 excursion intervals, the following criteria were used: (1) NRM demagnetization data of
291 the samples plotted on orthogonal projections show magnetization component with
292 inclination deviating >~45° from the expected values within a polarity chron (bottom
293 three panels in Figure 4); (2) there is no record of sampling disturbance or visible
294 changes in lithology; (3) similar paleomagnetic directional changes can be observed in
295 shipboard data and/or in samples from other holes over the same depth (mcd) interval; (4)
296 RPI estimates across the excursion interval have low values compared to surrounding
297 intervals; and (5) deconvolution of measurement data using UDECON (Oda and Xuan,
298 2014; Xuan and Oda, 2015) suggests that anomalous directions are not due to artifacts of
299 negative lobes in the SRM sensor response (Roberts, 2006). An example comparison of

300 ChRM directions (for core section U1304B-18H-3A) calculated using original and
301 deconvolved measurement data is shown in Supplementary Figure 1.
302
303 Excursion I (149.23-149.34 mcd) corresponds to the MIS 22/23 transition (Figure 3) and
304 is dated to between 885.84 and 889.22 ka (center age ~887.97 ka) (Table 2). This part of
305 the Site U1304 age model is based on correlation of benthic $\delta^{18}O$ to the LR04 stack.
306 Excursion I is recorded in core sections U1304A-14H-5 (at ~20 cm) and U1304B-15H-2
307 (near section top). ChRM directions (estimated from 20-80 mT interval) are significantly
308 shallower than values from surrounding intervals, and have large MAD values (Figure 3).
309 NRM demagnetization data in this interval have an apparent positive inclination
310 component at ~55-100 mT peak AF demagnetization, with a shallow negative inclination
311 overprint in the ~20-55 mT demagnetization interval (third row, Figure 4). Excursion I
312 occurs between the top of the Jaramillo Subchron and the Matuyama/Brunhes boundary.
313 Only two geomagnetic excursions have been documented within this time interval (Laj
314 and Channell, 2007): the Santa Rosa excursion and the Kamikatsura Excursion with
315 reported $^{40}Ar/^{39}Ar$ ages of ~936 ka and ~899 ka (Singer et al., 2004), respectively. The
316 Site U1304 benthic $\delta^{18}O$ based age of ~888 ka for Excursion I is close to that of the
317 Kamikatsura Excursion, which was first documented in the Kamikatsura Tuff of the
318 Osaka group in SW Japan (Maenaka, 1983), and has been reported in loess sections from
319 China (Yang et al., 2004; Wang et al., 2010; Ao et al., 2012; Liu et al., 2015), and in
320 marine sediments from the equatorial Pacific Ocean (Laj et al., 1996). An interval of
321 anomalously low virtual geomagnetic pole (VGP) latitudes also occurs at ODP Site 983
322 in MIS 21 at ~850 ka (Channell and Kleiven, 2000). Because of poor age control in

some of the marine sediment records (e.g. Laj et al., 1996), and delayed NRM acquisition in Chinese loess (e.g. Spassov et al., 2003) the existence of the Kamikatsura Excursion remains controversial. Singer et al. (1999) and Coe et al. (2004) considered that intermediate directions in the Haleakala Caldera (Maui), immediately below the Matuyama-Brunhes boundary, record the Kamakatsura excursion, although this is also controversial. The Santa Rosa excursion is, however, better defined both in igneous rocks (Singer and Brown, 2002) and in sedimentary sequences from the North Atlantic Ocean (Channell et al., 2002) and from the western Pacific Ocean (Horng et al., 2002, 2003).

Excursion II (~182.96-183.02 mcd) occurs between the top of the Cobb Mountain Subchron and the base of the Jaramillo Subchron (Figure 3), with an estimated age of ~1124 ka (Table 2). This excursion is recorded in core section U1304B-18H-3 (at ~80 cm). ChRM inclinations are significantly shallower (fourth row of Figure 4) than values in surrounding intervals and have large MAD values (Figure 3). The estimated age of ~1124 ka for Excursion II is close to the previously reported Punaruu Excursion from basaltic lava flows in the Punaruu Valley, Tahiti (Chauvin et al., 1990). $^{40}Ar/^{39}Ar$ methods yielded estimated ages of ~1105 ka (Singer et al., 1999) and ~1122 ka (Singer et al., 2004) for the Punaruu Excursion. Marine sediments from California Margin ODP Site 1021 (Guyodo et al., 1999), and North Atlantic ODP Sites 983 and 984 (Channell et al., 2002) and IODP Sites U1308 (Channell et al., 2008; 2016) also record this excursion, with estimated ages of 1110 ka (ODP Site 1021), 1115 ka (ODP Site 983 and 984) and 1092 ka (IODP Site U1308).

346 Excursion III (~220.75-221.18 mcd) is recorded below the Cobb Mountain Subchron
347 with an estimated age of ~1463 ka (Table 2). This excursion is recorded in core sections
348 U1304B-22H-2 (~100 cm) (Figure 3; and bottom row, Figure 4), U1304A-22H-1, and
349 U1304D-16H-6. In Supplementary Figure 2a and b, we compare shipboard NRM
350 inclinations and declinations from intervals that record the excursion, along with u-
351 channel data from Core U1304B-22H. Data from Cores U1304A-22H and U1304D-16H
352 were shifted down-section by 20 cm and 5 cm, respectively, relative to Core U1304B-
353 22H to optimize the correlation of shipboard susceptibility (Supplementary Figure 2c)
354 and natural gamma radiation data (Supplementary Figure 2d). The three records correlate
355 satisfactorily, notwithstanding erratic declinations in the excursion interval
356 (Supplementary Figure 2a and b). The estimated age of ~1463 ka for Excursion III is
357 close to the reported age of ~1472-1480 ka for the Gardar Excursion, which was first
358 documented at ODP Sites 983 and 984 (Channell et al., 2002). The Gardar Excursion has
359 also been reported in (paleo) lake sediments from SW China (An et al., 2011) and in a
360 loess section from North China (Ao et al., 2012).
361
362 *4.2 Diatom Deposition and its Influence on Paleomagnetic records*
363 Rock magnetic data (κ, ARM, and IRM) are shown in Figure 5 together with the spliced
364 core image of the sampled composite section, shipboard counts of diatom percentage per
365 core section (Expedition 303 Scientists, 2006) and abundance of the dominant diatom
366 species *Thalassiothrix longissima* (Shimada et al., 2008). Susceptibility (κ), as well as
367 ARM and IRM intensities indicate the concentration of magnetic minerals (mainly
368 magnetite), and are sensitive to different grain-size populations of magnetic grains.

369 Variations in these parameters at Site U1304 are closely related to diatom abundance.
370 Susceptibility, ARM, and IRM values from diatom-rich sediment (vertical gray bars in
371 Figure 5) are usually 1->2 orders of magnitude lower than those from non-diatom-rich
372 intervals. In addition, within diatom-rich intervals with higher diatom mat abundances
373 (DRV=1, vertical dark gray bars in Figure 5), we observe lower values of susceptibility,
374 ARM, and IRM. For instance, the lowest values of these magnetic parameters occur at
375 ~44-49, 55-60 mcd, 94-107 mcd and 194-203 mcd where the thickest diatom mats are
376 observed (Figure 5). S-ratios also co-vary with diatom occurrence (Figure 5f), with
377 diatom-rich intervals often having lower values of ~0.9 while non-diatom-rich sediment
378 has values close to 1. The lower S-ratios suggest that diatom-rich sediment contains
379 higher coercivity magnetic minerals. This is consistent with NRM demagnetization
380 behavior (second row, Figure 4), where samples from diatom-rich intervals often have
381 more NRM remaining after 100-mT demagnetization compared to non-diatom-rich
382 intervals (top row, Figure 4).
383
384 Hysteresis ratios on a Day et al. (1977) plot are shown in Figure 6a. Data symbols for the
385 hysteresis ratios are color-coded by the mean value of susceptibility (κ) within the core
386 section, which can be used to estimate diatom-richness. All hysteresis ratio data lie in the
387 pseudo single domain (PSD) region on the Day et al. (1977) plot with a distribution
388 elongated along a typical magnetite grain-size mixing trend. No apparent difference in
389 magnetic grain size is observed between samples from diatom-rich (low κ) and non-
390 diatom-rich intervals (high κ). Hysteresis ratios from the low κ (yellow) intervals appear
391 to lie on a slightly different grain-size mixing line toward higher H_{cr}/H_c values, which is

392 consistent with the presence of a higher-coercivity magnetic mineral in the diatom-rich
393 sediments. Representative hysteresis loops and back-field remanence measurements for
394 non-diatom-rich samples have typical characteristics of a low-coercivity magnetic
395 mineral with a paramagnetic component (Figure 6b, c). Hysteresis loops and back-field
396 remanence data for diatom-rich sediments are nosier due to the low magnetic mineral
397 concentration (Figure 6d, e), and the saturation field and remanent coercivity (H_{cr}) are
398 apparently larger than those of non-diatom-rich sediments.
399
400 To test if the low concentration and presence of high-coercivity magnetic minerals in
401 diatom-rich intervals influences paleomagnetic directions, magnetization intensities and
402 RPI records, we compare histograms of paleomagnetic data from non-diatom-rich and
403 diatom-rich sediments (Figure 7). NRM intensities (after 35-mT demagnetization) of
404 diatom-rich samples have distinctly different distribution from non-diatom-rich samples
405 with variable value from below 10^{-4} A/m to ~10^{-1} A/m (Figure 7a). Despite the apparent
406 difference in NRM intensity, ChRM directions (Figure 7b, c) from non-diatom-rich and
407 diatom-rich samples are comparable to each other. Corrected ChRM declinations from
408 both non-diatom-rich and diatom-rich intervals are around 0° (or 360°) and 180° with a
409 similar distribution, although data from diatom-rich intervals appear to have slightly
410 greater spread over the data range. Similarly, ChRM inclinations from non-diatom-rich
411 and diatom-rich sediments have comparable distributions for normal (positive
412 inclinations) and reverse (negative inclinations) polarity chrons. ChRM inclinations from
413 diatom-rich intervals appear to be slightly shallower (by ~4°-5°) and more scattered than

414 for non-diatom-rich intervals (mean values of ChRM inclinations are ~64.7° and ~-60.6°
415 for non-diatom-rich sediments, and ~60.7° and ~-55.1° for diatom-rich sediments).
416
417 Histograms of r-values (linear correlation coefficients) associated with RPI estimates for
418 slopes of best-fit lines between NRM intensity lost versus (1) ARM lost, (2) ARM
419 acquired, and (3) IRM lost are shown in Figure 7d. The optimal normalizer for RPI
420 proxies should activate the same population of magnetic grains that carry the NRM (e.g.
421 Levi and Banerjee, 1976), so that demagnetization or acquisition behaviour of the
422 normalizer should mimic that of the NRM demagnetization, with a similar proportion of
423 magnetization lost or acquired between the same treatment levels, resulting in r-values
424 close to 1. RPI estimates using NRM lost versus ARM acquired appear to be associated
425 with the largest r-values that are close to 1 (green vertical bars in Figure 7d). Using only
426 r-values that are larger than 0.98, mean r-values are 0.9948, 0.9984, and 0.9967 for RPI
427 estimates using NRM lost versus ARM lost, NRM lost versus ARM acquired, and NRM
428 lost versus IRM lost, respectively.
429
430 RPI estimates and associated r-values using NRM lost versus ARM lost, and NRM lost
431 versus ARM acquired are plotted against mcd in Figure 8. The two RPI estimates are
432 comparable (bottom panel, Figure 8), with r-values for NRM lost versus ARM acquired
433 (red points, top panel in Figure 8) having consistently higher (closer to 1) values for
434 almost the entire studied depth interval. We, therefore, estimated RPI using slopes of
435 best-fit lines of NRM lost versus ARM acquired for Site U1304. Histograms of ARM
436 intensity (after 35-mT demagnetization with 50-μT DC bias field) and RPI estimates

437 using NRM lost versus ARM acquired for both non-diatom-rich and diatom-rich samples
438 are compared in Figure 7e and f. Similar to the NRM intensity data (Figure 7a),
439 distributions of the ARM intensity data for non-diatom-rich and diatom-rich samples are
440 different, with data from non-diatom-rich samples having a broader distribution of values
441 (Figure 7e). Despite distinct distributions of NRM and ARM intensity data, RPI estimates
442 from the non-diatom-rich and diatom-rich samples have similar distributions and both
443 have mean values around 0.35 (Figure 7f), which suggests that although diatoms decrease
444 the magnetic mineral concentration, RPI proxies are not affected significantly. We also
445 note that RPI from diatom-rich sediments contain slightly more values >1 compared with
446 RPI estimations from non-diatom-rich sediments that contain few such values. These
447 large RPI values in diatom-rich intervals give rise to spikes in Figure 8, and could be
448 related to inadequate normalization. We further refined our RPI record by discarding RPI
449 estimates, based on NRM lost versus ARM acquired, using two criteria: (1) r-values
450 <0.98; or (2) raw RPI (slope) values >1. The resulting RPI record for Site U1304 against
451 age is shown in Figure 9f. The satisfactory correlation between the Site U1304 RPI
452 record and the PISO-1500 RPI stack (Channell et al., 2009) for both the non-diatom-rich
453 and the diatom-rich intervals (Figure 9f) further suggest that RPI estimates are not
454 significantly degraded by diatom-rich intervals. In addition, no apparent correlation is
455 observed between RPI (Figure 9f) and the "normalizer" ARM; Figure 9a).
456
457 The close relationship between magnetic concentration dependant parameters and
458 diatom-richness means that magnetic data can potentially serve as a high-resolution bulk
459 diatom abundance proxy at Site U1304. Reduced magnetic mineral concentration during

460 diatom-rich intervals is attributed to dilution caused by rapid diatom deposition. Diatom-
461 rich sediments generally have elevated mean sedimentation rates of ~20 to over 30
462 cm/kyr (Figure 9c). Observation of laminated diatom deposits in the deep-sea was first
463 documented in Neogene sediments of the eastern equatorial Pacific Ocean (Kemp and
464 Baldauf, 1993) and later in Pleistocene sediments at ODP Site 1093 in the South Atlantic
465 (Grigorov et al., 2002). Apart from IODP Site U1304 (Expedition 303 Scientists, 2006;
466 Shimada et al., 2008; Romero et al., 2011), the only report of laminated diatom-rich
467 sediments in the deep North Atlantic Ocean was during MIS 5 in a short piston core
468 EW9303-17 (Bodén and Backman, 1996), located ~500 km NNW of Site U1304 (Figure
469 1). Accumulations of laminated diatom-rich sediments in the deep-sea are often
470 associated with the convergence of major oceanic frontal systems. Bodén and Backman
471 (1996) explained the occurrence of laminated diatom-rich sediments in Core EW9303-17
472 as related to the position of the subarctic convergence where the warm and saline North
473 Atlantic and Irminger Currents meet the cold and less saline Labrador Sea water. This
474 hypothesis was supported by Shimada et al. (2008) in explaining the occurrence of
475 laminated diatom-rich sediments at Site U1304. Romero et al. (2011) argued that the
476 subarctic convergence alone is insufficient to provide the necessary nutrients to sustain
477 the observed diatom productivity at Site U1304, and that incursions of silicate- and
478 nitrate-rich subantarctic mode water due to slowdown of Iceland-Scotland overflow
479 water, and sporadic convective mixing of the water column might have played a decisive
480 role.
481

Based on a chronology constructed using shipboard polarity stratigraphy and biostratigraphy, Shimada et al. (2008) noted that diatom occurrence at Site U1304 is not simply related to glacial-interglacial cycles. For the last interglacial, Romero et al. (2011) observed peak abundance of diatom mats at the MIS 5d/5e boundary at ~116 ka. According to the updated age model (Table 1), diatom mat deposition tends to occur late in interglacial stages and during glacial inception, rather than in peak interglacials, but not in all interglacials, as well as in the weak glacial of MIS 14 (Figure 9). Minor deposition of diatom mats occurred in some interglacials (e.g. MIS 49, 37, 33, 31, 23, 19, and 17). For the last ~1.5 Myr, the most prominent episodes of diatom mat deposition at Site U1304 occurred at around MIS 39, during MIS 35, 27, 21, between MIS 15 and 13, including MIS 14, and during MIS 11 and 9. The increase in the occurrence of diatom mats during the middle Brunhes Chron (between MIS 9 and 15) at Site U1304 may coincide with an increase in pelagic carbonate production at this time (Barker et al., 2006).

Preservation of laminated diatom mats often requires inhibition of benthos by low dissolved oxygen levels either in anoxic basins (e.g. Schimmelmann and Lange, 1996) or beneath areas of coastal upwelling (e.g. Brodie and Kemp, 1994). On the other hand, where the deep-sea was well oxygenated, preservation of laminated diatom mats cannot be attributed to low oxygen levels. The absence of bioturbation in laminated intervals can be explained by physical suppression of benthic faunal burrowers because of the high tensile strength of diatom mats (Kemp and Baldauf, 1993). High rates of sediment accumulation and low bioturbation in diatom mats result in high stratigraphic resolution.

505 We speculate that the lower density (Expedition 303 Scientists, 2006) and mesh-like
506 structure of the diatom mats, and the physical suppression of benthic activity beneath the
507 laminated intervals promoted a slightly more oxic environment within diatom-rich
508 intervals shortly after deposition, whereby fine PSD magnetite particles experienced
509 certain degree of oxidation that produced higher coercivity magnetic minerals such as
510 maghemite (Kawamura et al., 2012). This process would explain the presence of high
511 coercivity magnetic components in the diatom-rich sediments as indicated by the NRM
512 demagnetization behavior, S-ratios, and hysteresis parameters. Compaction, de-watering
513 and the lack of bioturbation of diatom-rich sediments after deposition may have led to the
514 slightly shallower inclinations (~4-5°) observed in the diatom-rich sediments (Figure 7c).
515
516 *4.3 High-resolution North Atlantic Paleointensity Stack (HINAPIS-1500) and Wavelet*
517 *Analyses of RPI Records*
518 In Figure 10a, we compare the Site U1304 RPI record with other individual RPI records
519 that cover the last 1.5 Myr with mean sedimentation rates >10 cm/kyr. Only three such
520 records exist and all are from the northern North Atlantic Ocean (Figure 1): ODP Sites
521 983 and 984 (Channell et al., 1997, 2002; Channell, 1999; Channell and Kleiven, 2000),
522 and IODP Site U1306 (Channell et al., 2014). RPI records from ODP Sites 983 and 984,
523 and IODP Sites U1304 and U1306 were used to construct a high-resolution stack record.
524 Construction of the RPI stack (here named "HINAPIS-1500") follows new procedures
525 from those used for PISO-1500 (Channell et al., 2009), SINT-800 (Guyodo and Valet,
526 1999), and SINT-2000 (Valet et al., 2005). To allow for more realistic uncertainty
527 estimates, individual records are placed on their published age models without

528 correlation/matching to a target record or interpolation of records onto a common age
529 model. All records were normalized to their means for the same 0-1500 ka time interval.
530 This procedure is necessary to account for differences in normalization parameter/method
531 used for RPI estimation, and for possible differences in paleointensity at different
532 locations. The new stack was constructed for time-steps between 0 and 1500.5 ka at 0.5
533 kyr intervals (i.e. 0.5, 1, 1.5, …, 1499, 1499.5, 1500). For each time step center (t_i), RPI
534 values were randomly drawn (10,000 times with a uniform distribution) within the t_i-0.5
535 to the t_i+0.5 time interval (1-kyr duration) from the four records (2,500 times from each
536 record to ensure equal weight for each record). This process allows a 0.5 kyr overlapping
537 interval within which RPI values are drawn when constructing the stack for each adjacent
538 time step. Chronological uncertainty certainly exceeds 0.5 kyr. Allowance of a 0.5-kyr
539 overlapping interval for stacking is therefore justified while making available more RPI
540 values for the bootstrap experiment at each time step (usually ~5 to over 20 data points
541 from each record in the stack; Figure 10c). For each time step, the mean of the 10,000 (or
542 less for occasional intervals where some records do not have RPI values) randomly
543 drawn RPI values was used to produce the stack (red curve in Figure 10b). We estimated
544 the 90% confidence level (vertical gray intervals in Figure 10b) for each stacked value
545 using cut-off levels of the top and bottom 5% of randomly drawn RPI values at each time
546 step.
547
548 The HINAPIS-1500 RPI stack compares well with the published PISO-1500 RPI stack on
549 time scales of a few thousand to tens of thousands of years (Figure 10b). The apparent
550 mismatch between ~630 and 700 ka is probably caused by age model discrepancies. Age

551 models for ODP Sites 983 and 984, and IODP Site U1304 during this interval are based
552 on oxygen isotope stratigraphy, while the IODP Site U1306 record for this interval was
553 dated through tandem correlation of both RPI and oxygen isotope to the PISO-1500 and
554 the LR04 stacks (Channell et al., 2014). The ODP Site 983 and 984 RPI records used in
555 the HINAPIS-1500 stack were also used for PISO-1500 RPI stack construction, although
556 the PISO-1500 stack included 11 other records including 2 from the western equatorial
557 Pacific Ocean, 1 from the Indian Ocean, and 1 from the South Atlantic Ocean. Within the
558 0-1500 ka time interval, 9 out of the 13 records in PISO-1500 spanned ~500 kyr or
559 longer, among which 6 spanned ~1000 kyr or longer. It is possible that spatial bias of the
560 records in PISO-1500 toward the North Atlantic (9 of 13) may contribute to the observed
561 correlation between HINAPIS-1500 and PISO-1500, which are both dominated by
562 common paleointensity variability in the North Atlantic region. The PISO-1500 RPI stack
563 fits within the 90% confidence intervals of the HINAPIS-1500 record (Figure 10b). The
564 observation that a regional (northern North Atlantic) RPI stack (i.e. HINAPIS-1500) can
565 be correlated satisfactorily to another stack built using globally distributed records (i.e.
566 PISO-1500) suggest that RPI variations are global on times scales of a few tens of
567 thousand years, and therefore can be used as a valuable high-resolution and independent
568 global stratigraphic correlation and dating tool.
569
570 To further investigate common variability among the individual records and RPI stacks,
571 and the time-frequency domain characteristics of the records, wavelet analyses including
572 local wavelet power spectra (LWPS), global wavelet power spectra (GWPS), and wavelet
573 coherence (WTC) (Torrence and Compo, 1998; Torrence and Webster, 1999; Grinsted et

al., 2004) were performed on the Site U1304 RPI record, and the HINAPIS-1500 and PISO-1500 stacks, and on other individual records used in the HINAPIS-1500 stack. During the last two decades, orbital cycles with ~100 kyr and/or ~41 kyr periods, have been reported in RPI records from marine sediments and have been considered evidence for orbital forcing on the geodynamo (e.g. Channell et al., 1998; Yamazaki, 1999; Yamazaki and Oda, 2002; Thouveny et al., 2004; 2008). On the other hand, wavelet analyses of some of these records indicated that orbital periods in the RPI record are possibly due to lithological variations (Guyodo et al., 2000) or are not statistically significant (Roberts et al., 2003). Based on analyses of multiple records from both the Atlantic and Pacific Oceans, Xuan and Channell (2008) suggested that orbital periods are introduced into NRM records through orbital control on subtle lithologic variations. Our analyses of the Site U1304, HINAPIS-1500, and PISO-1500 RPI data using LWPS (Supplementary Figure 3a-c) indicate little significant (1% level against red noise) power at orbital periods in these records. The apparent high power for the 41-kyr period at ~700 ka and ~1100 ka in the HINAPIS-1500 stack (Supplementary Figure 3b) are likely due to strong obliquity power in RPI data from ODP Site 983 during these time intervals (Figure 4a in Xuan and Channell, 2008). The lack of significant orbital power in the analyzed RPI records is consistent with the suggestion that orbital periods observed in some individual RPI records are due to lithological contamination (Guyodo et al., 2000; Xuan and Channell, 2008).

The definition of squared WTC closely resembles that of a traditional correlation coefficient, and it is useful to think of the WTC as a localized correlation coefficient in

time-frequency (or -period) space (Grinsted et al., 2004). Squared WTC between the Site U1304 RPI record and the HINAPIS-1500 stack (Supplementary Figure 3g) indicate significant coherence at periods ranging from ~8 kyr to over 500 kyr during various time intervals. The two records appear to be coherent with one another at periods of ~64-100 kyr and at around 256 kyr, for majority of the 0-1500 ka time interval. Similar WTC is observed between the Site U1304 RPI record and the PISO-1500 stack (Supplementary Figure 3i). The fact that the two records are more coherent with each other beyond ~1000 ka is probably because the Site U1304 age model beyond 1000 ka was based on automated matching of Site U1304 RPI to the PISO-1500 stack. During the ~0-300 ka time interval, Site U1304 RPI has a larger and more significant coherence with the HINAPIS-1500 stack than the PISO-1500 stack on periods ranging between ~8 kyr and ~20 kyr. This is reflected in the lack of coherence on the WTC map between the PISO-1500 and the HINAPIS-1500 stack (Supplementary Figure 3h) over the same period. Significant coherence between the PISO-1500 and HINAPIS-1500 stacks over the majority of the time-period space at periods above ~40 kyr is consistent with the observed correlation of the two records in the time domain (Figure 10b). Significant WTC of the two stack records can also be seen for periods between ~8 and 40 kyr for multiple time intervals (Supplementary Figure 3h). The lack of significant WTC between any of the three records for periods of <~8 kyr is likely related to chronological uncertainties in these records, which could reach a few kyr and affect analyses of short-term variability. The two period ranges over which all three RPI records appear to be coherent with each other are periods between ~64 and 100 kyr and around 256 kyr. These two ranges are also dominant peaks in the global wavelet power spectra (GWPS) of these

620 records (Supplementary Figure 3d-e), which sum the wavelet power along the time axis
621 for each frequency (or period) component. The coherent high power of variability over
622 the two ranges of periods appear to be a common feature for RPI records and could
623 potentially relate to mechanisms that drive the geodynamo.
624
625 **5. Conclusions**
626 An age model for the sediment sequence at IODP Site U1304 for the last ~1.5 Myr was
627 based on: (1) correlation of Site U1304 magnetic susceptibility to that of Core JPC-13,
628 from the same location, for the 0-125 ka interval, and use of the benthic $\delta^{18}O$-based age
629 model of Core JPC-13 (Hodell et al., 2010); (2) correlation of the Site U1304 benthic
630 $\delta^{18}O$ record to the LR04 $\delta^{18}O$ stack from ~125 ka to ~1 Ma; and (3) automated matching
631 of the Site U1304 RPI record to the PISO-1500 RPI stack for the ~1-1.5 Ma interval.
632 ChRM declination and inclination data from u-channel measurements reveal
633 unambiguously the Matuyama-Brunhes boundary (at ~138.98 mcd), the Jaramillo
634 Subchron (at ~164.63-176.04 mcd), and the Cobb Mountain Subchron (at ~188.17-
635 191.54 mcd), with estimated ages of ~772 ka, ~993-1071 ka, and ~1193-1219 ka,
636 respectively. Three geomagnetic excursions are observed at Site U1304 in the Matuyama
637 Chron at ~888 ka, ~1124 ka, and ~1463 ka. These magnetic excursions may be correlated
638 to previously documented "Kamikatsura/Santa Rosa", "Punaruu", and "Gardar"
639 excursions with similar reported ages.
640
641 Diatom mats at Site U1304 are associated with elevated sedimentation rates, and
642 generally occur in the latter part of certain interglacial stages and during glacial

643 inceptions. Prominent episodes of diatom mat deposition occurred in the latter part of
644 MIS 39, 35, 27, 21, between MIS 15 and 13, including the weak glacial MIS 14, and
645 during the latter part of MIS 11 and 9. As expected, rapid deposition of diatom mats at
646 Site U1304 appears to have substantially diluted the concentration of magnetic minerals,
647 leading to much lower volume susceptibility, ARM intensity, and IRM intensity in
648 diatom-rich intervals. A high coercivity magnetic component is preserved in the diatom-
649 rich sediments, possibly maghemite. Maghematization could have occurred due to
650 oxidation of fine PSD magnetite in diatom-rich layers due to a slightly more oxic
651 environment created by a combination of lower density mesh-like diatom mats and
652 physical suppression of benthic activity within diatom-rich layers shortly after deposition.
653 Despite the much weaker magnetizations, and possible occurrence of high coercivity
654 minerals, comparison of histograms of paleomagnetic data from both non-diatom-rich
655 and diatom-rich sediments indicates that the diatom mats do not significantly degrade the
656 fidelity of paleomagnetic directions or RPI proxies. Slightly shallower inclinations (~4-
657 5°) in the diatom-rich sediments could be related to compaction, de-watering, and lack of
658 bioturbation of diatom-rich sediments.
659
660 The Site U1304 RPI record correlates with the PISO-1500 RPI stack and with three other
661 North Atlantic records (ODP Sites 983 and 984, and IODP Site U1306) that span the last
662 1500 kyr at similar resolution (i.e. mean sedimentation rates >10 cm/kyr). These three
663 records were used together with the Site U1304 RPI record to build a high-resolution
664 reference paleointensity stack (HINAPIS-1500) for the northern North Atlantic region,
665 following a new stacking method. The HINAPS-1500 stack matches the PISO-1500 stack

666 on time scales greater than a few thousand years. Wavelet analyses of the Site U1304 RPI
667 record, HINAPIS-1500, and PISO-1500, indicate no statistically significant power at
668 orbital periods, in agreement with previous suggestions that orbital periods observed in
669 some individual RPI records are due to lithological contamination rather than to orbital
670 forcing of the geodynamo. Squared wavelet coherence and global wavelet power spectra
671 of individual RPI records and stacks have very high coherence and global power at period
672 bands of ~64-100 kyr and around 256 kyr, which might constitute a common feature
673 associated with RPI variations.
674

675 **Acknowledgements**

676 We thank Jason Curtis and Gianna Browne for processing of samples for stable isotope
677 analyses, and Kainian Huang for assistance in the paleomagnetic laboratory. We
678 gratefully acknowledge assistance from the scientific party and crew of R/V *JOIDES*
679 *Resolution* during IODP Expedition 303, and from the curatorial staff at the IODP core
680 repository in Bremen. Alain Mazaud, Joe Stoner, and Helen Evans helped with u-channel
681 sampling. Research funded by NSF grants 0850413 and 1014506 to Channell and NERC
682 grant NE/H009930/1 to Hodell. The HINAPIS-1500 stack is archived as Supplementary
683 Data with this article, and other relevant data are archived in the Pangaea Database.
684

685 References

686 An, Z., Clemens, S.C., Shen, J., Qiang, X., Jin, Z., Sun, Y., Prell, W.L., Luo, J., Wang,
687 S., Xu, H., 2011. Glacial-interglacial Indian summer monsoon dynamics. Science
688 333, 719-723.

689 Ao, H., An, Z., Dekkers, M.J., Wei, Q., Pei, S., Zhao, H., Zhao, H., Xiao, G., Qiang, X.,
690 Wu, D., 2012. High-resolution record of geomagnetic excursions in the Matuyama
691 chron constrains the ages of the Feiliang and Lanpo Paleolithic sites in the Nihewan
692 Basin, North China. Geochem. Geophys. Geosyst., 13, Q08017,
693 doi:10.1029/2012GC004095.
694 Barker, S., Archer, D., Booth, L., Elderfield, H., Henderiks, J., Rickaby, R.E.M., 2006.
695 Globally increased pelagic carbonate production during the Mid-Brunhes dissolution
696 interval and the CO_2 paradox of MIS 11. Quat. Sci. Rev. 25, 3278-3293.
697 Bloemendal, J., King, J.W., Hall, F.R., Doh, S.J., 1992. Rock magnetism of late Neogene
698 and Pleistocene deep-sea sediments - relationship to sediment source, diagenetic
699 processes, and sediment lithology. J. Geophys. Res. 97, 4361-4375.
700 Boden, P., Backman, J., 1996. A laminated sediment sequence from the northern North
701 Atlantic Ocean and its climatic record. Geology 24, 507-510.
702 Brodie, I., Kemp, A.E.S., 1994. Variation in biogenic and detrital fluxes and formation of
703 laminae in late Quaternary sediments from the Peruvian coastal upwelling zone. Mar.
704 Geol. 116, 385-398.
705 Channell, J.E.T., 1999. Geomagnetic paleointensity and directional secular variation at
706 Ocean Drilling Program (ODP) Site 984 (Bjorn Drift) since 500 ka: comparisons
707 with ODP Site 983 (Gardar Drift). J. Geophys. Res. 104, 22,937-922,951.
708 Channell, J.E.T., Hodell, D.A., Lehman, B., 1997. Relative geomagnetic paleointensity
709 and $\delta^{18}O$ at ODP Site 983 (Gardar Drift, North Atlantic) since 350 ka. Earth Planet.
710 Sci. Lett. 153, 103-118.

711 Channell, J.E.T., Hodell, D.A., McManus, J., Lehman, B., 1998. Orbital modulation of
712 the Earth's magnetic field intensity. Nature 394, 464-468.
713 Channell, J.E.T., Hodell, D.A., Xuan, C., Mazaud, A., Stoner, J.S., 2008. Age calibrated
714 relative paleointensity for the last 1.5 Myr at IODP Site U1308 (North Atlantic).
715 Earth Planet. Sci. Lett. 274, 59-71.
716 Channell, J.E.T., Kleiven, H.F., 2000. Geomagnetic palaeointensities and
717 astrochronological ages for the Matuyama-Brunhes boundary and the boundaries of
718 the Jaramillo Subchron: palaeomagnetic and oxygen isotope records from ODP Site
719 983. Philos. Trans. R. Soc. Lond. Ser. A 358, 1027-1047.
720 Channell, J.E.T., Mazaud, A., Sullivan, P., Turner, S., Raymo, M.E., 2002. Geomagnetic
721 excursions and paleointensities in the Matuyama Chron at Ocean Drilling Program
722 Sites 983 and 984 (Iceland Basin). J. Geophys. Res. 107, 2114,
723 doi:2110.1029/2001JB000491.
724 Channell, J.E.T., Wright, J.D., Mazaud, A., Stoner, J.S., 2014. Age through tandem
725 correlation of Quaternary relative paleointensity (RPI) and oxygen isotope data at
726 IODP Site U1306 (Eirik Drift, SW Greenland). Quat. Sci. Rev. 88, 135-146.
727 Channell, J.E.T., Xuan, C., Hodell, D.A., 2009. Stacking paleointensity and oxygen
728 isotope data for the last 1.5 Myr (PISO-1500). Earth Planet. Sci. Lett. 283, 14-23.
729 Channell, J.E.T., Hodell, D.A., Curtis, J.H., 2016. Relative paleointensity (RPI) and
730 oxygen isotope stratigraphy at IODP Site U1308: North Atlantic RPI stack for 1.2-
731 2.2 Ma (NARPI-2200) and age of the Olduvai Subchron. Quaternary Science
732 Reviews, 131, 1-19.

733 Chauvin, A., Roperch, P., Duncan, R.A., 1990. Records of geomagnetic reversals from
734 volcanic islands of French Polynesia 2. Paleomagnetic study of a flow sequence (1.2-
735 0.6 Ma) from the island of Tahiti and discussion of reversal models. J. Geophys. Res.
736 95(B3), 2727–2752, doi:10.1029/JB095iB03p02727.
737 Coe, R.S., Singer, B.S., Pringle, M.S., Zhao, X., 2004. Matuyama–Brunhes reversal and
738 Kamikatsura event on Maui: paleomagnetic directions, 40Ar/39Ar ages and
739 implications. Earth Planet. Sci. Lett. 222, 667-684.
740 Day, R., Fuller, M., Schmidt, V.A., 1977. Hysteresis properties of titanomagnetites:
741 grain-size and compositional dependence. Phys. Earth Planet. Inter. 13, 260-267.
742 Evans, H.F., 2006. Magnetic stratigraphy and environmental magnetism of oceanic
743 sediments. PhD diss., University of Florida.
744 Galaasen, E.V., Ninnemann, U.S., Irvalı, N., Kleiven, H.F., Rosenthal, Y., Kissel, C.,
745 Hodell, D.A., 2014. Rapid Reductions in North Atlantic Deep Water During the Peak
746 of the Last Interglacial Period. Science 343, 1129-1132.
747 Grigorov, I., Pearce, R.B., Kemp, A.E.S., 2002. Southern Ocean laminated diatom ooze:
748 mat deposits and potential for palaeo-flux studies, ODP leg 177, Site 1093. Deep-Sea
749 Res. Part II-Top. Stud. Oceanogr. 49, 3391-3407.
750 Grinsted, A., Moore, J.C., Jevrejeva, S., 2004. Application of the cross wavelet transform
751 and wavelet coherence to geophysical time series. Nonlinear Proc. Geophys. 11, 561-
752 566.
753 Guyodo, Y., Gaillot, P., Channell, J.E.T., 2000. Wavelet analysis of relative geomagnetic
754 paleointensity at ODP Site 983. Earth Planet. Sci. Lett. 184, 109-123.

755 Guyodo, Y., Richter, C., Valet, J.P., 1999. Paleointensity record from Pleistocene
756 sediments (1.4-0 Ma) off the California Margin. J. Geophys. Res. 104, 22953-22964.
757 Guyodo, Y., Valet, J.P., 1999. Global changes in intensity of the Earth's magnetic field
758 during the past 800 kyr. Nature 399, 249-252.
759 Hodell, D.A., Evans, H.F., Channell, J.E.T., Curtis, J.H., 2010. Phase relationships of
760 North Atlantic ice-rafted debris and surface-deep climate proxies during the last
761 glacial period. Quat. Sci. Rev. 29, 3875-3886.
762 Hodell, D.A., Minth, E.K., Curtis, J.H., McCave, I.N., Hall, I.R., Channell, J.E.T., Xuan,
763 C., 2009. Surface and deep-water hydrography on Gardar Drift (Iceland Basin)
764 during the last interglacial period. Earth Planet. Sci. Lett. 288, 10-19.
765 Horng, C.S., Lee, M.Y., Palike, H., Wei, K.Y., Liang, W.T., 2002. Astronomically
766 calibrated ages for geomagnetic reversals within the Matuyama chron. Earth, Planets
767 and Space 54, 679-690.
768 Horng, C.S., Roberts, A.P., Liang, W.T., 2003. A 2.14-Myr astronomically tuned record
769 of relative geomagnetic paleointensity from the western Philippine Sea. J. Geophys.
770 Res. 108.
771 Kawamura, N., N. Ishikawa, and M. Torii (2012), Diagenetic alteration of magnetic
772 minerals in Labrador Sea sediments (IODP Sites U1305, U1306, and U1307),
773 Geochem. Geophys. Geosyst. 13, Q08013, doi:10.1029/2012GC004213.
774 Kemp, A.E.S., Baldauf, J.G., 1993. Vast Neogene Laminated Diatom Mat Deposits from
775 the Eastern Equatorial Pacific-Ocean. Nature 362, 141-144.

776 King, J.W., Banerjee, S.K., Marvin, J., 1983. A new rock-magnetic approach to selecting
777 sediments for geomagnetic paleointensity studies; application to paleointensity for
778 the last 4000 years. J. Geophys. Res. 88, 5911-5921.
779 Kirschvink, J.L., 1980. The least-squares line and plane and the analysis of
780 paleomagnetic data. Geophys. J. Roy. Astron. Soc. 62, 699-718.
781 Laj, C., Channell, J.E.T., 2007. Geomagnetic Excursions, in: Schubert, G. (Ed.), Treatise
782 on Geophysics. Elsevier, Amsterdam, pp. 373-416.
783 Laj, C., Kissel, C., Beer, J., 2004. High Resolution Global Paleointensity Stack Since 75
784 kyr (GLOPIS-75) Calibrated to Absolute Values., in: Channell, J.E.T., Kent, D.V.,
785 Lowrie, W., Meert, J. (Eds.), Timescales of the Paleomagnetic field. AGU Geophys.
786 Monogr., pp. 255-266.
787 Laj, C., Kissel, C., Garnier, F., HerreroBervera, E., 1996. Relative geomagnetic field
788 intensity and reversals for the last 1.8 My from a central equatorial Pacific core.
789 Geophys. Res. Lett. 23, 3393-3396.
790 Levi, S., Banerjee, S.K., 1976. On the possibility of obtaining relative paleointensities
791 from lake sediments. Earth Planet. Sci. Lett. 29, 219-226.
792 Lisiecki, L.E., Lisiecki, P.A., 2002. Application of dynamic programming to the
793 correlation of paleoclimate records. Paleoceanography 17, 1049,
794 doi:1010.1029/2001PA000733.
795 Lisiecki, L.E., Raymo, M.E., 2005. A Pliocene-Pleistocene stack of 57 globally
796 distributed benthic $\delta^{18}O$ records. Paleoceanography 20, PA1003,
797 doi:10.1029/2004PA001071.

798 Liu, Q., Jin, C., Hu, P., Jiang, Z., Ge, K., Roberts, A.P., 2015. Magnetostratigraphy of
799 Chinese loess–paleosol sequences. Ear. Sci. Rev. 150, 139-167.
800 Maenaka, K., 1983. Magnetostratigraphic study of the Osaka group, with special
801 reference to the existence of pre and past-Jaramillo episodes in the late Matuyama
802 polarity Epoch. Mem. Hanazono Univ. 14, 1-65.
803 Nagy, E.A., Valet, J.P., 1993. New advances for paleomagnetic studies of sediment cores
804 using u-channels. Geophys. Res. Lett. 20, 671-674.
805 Oda, H., Xuan, C., 2014. Deconvolution of continuous paleomagnetic data from pass-
806 through magnetometer: A new algorithm to restore geomagnetic and environmental
807 information based on realistic optimization. Geochem. Geophys. Geosyst. 15, 3907-
808 3924.
809 Roberts, A.P., Winklhofer, M., Liang, W.-T., Horng, C.-S., 2003. Testing the hypothesis
810 of orbital (eccentricity) influence on Earth's magnetic field. Earth Planet. Sci. Lett.
811 216, 187-192.
812 Roberts, A.P., 2006. High-resolution magnetic analysis of sediment cores: Strengths,
813 limitations and strategies for maximizing the value of long-core magnetic data. Phys.
814 Earth Planet. Inter. 156, 162-178.
815 Roberts, A.P., 2008. Geomagnetic excursions: Knowns and unknowns. Geophys. Res.
816 Lett. 35, L17307, doi:10.1029/2008GL034719.
817 Romero, O.E., Swann, G.E.A., Hodell, D.A., Helmke, P., Rey, D., Rubio, B., 2011. A
818 highly productive Subarctic Atlantic during the Last Interglacial and the role of
819 diatoms. Geology 39, 1015-1018.

820 Ruddiman, W., Glover, L., 1975. Subpolar North Atlantic circulation at 9300 yr BP:
821 faunal evidence. Quat. Res. 5, 361-389.
822 Schimmelmann, A., Lange, C.B., 1996. Tales of 1001 varves: a review of Santa Barbara
823 Basin sediment studies. Geol. Soc. London Spec. Publ. 116, 121-141.
824 Scientists, E., 2006. Site U1304, in: Channell, J.E.T., Kanamatsu, T., Sato, T., Stein, R.,
825 Alvarez Zarikian, C.A., Malone, M.J., Scientists, E. (Eds.), Proc. IODP, 303/306,
826 College Station TX (Integrated Ocean Drilling Program Management International,
827 Inc.).
828 Shimada, C., Sato, T., Toyoshima, S., Yamasaki, M., Tanimura, Y., 2008.
829 Paleoecological significance of laminated diatomaceous oozes during the middle-to-
830 late Pleistocene, North Atlantic Ocean (IODP Site U1304). Mar. Micropaleontol. 69,
831 139-150.
832 Singer, B.S., Brown, L.L., 2002. The Santa Rosa Event: 40Ar/39Ar and paleomagnetic
833 results from the Valles rhyolite near Jaramillo Creek, Jemez Mountains, New
834 Mexico. Earth Planet. Sci. Lett. 197, 51-64.
835 Singer, B.S., Brown, L.L., Rabassa, J.O., Guillou, H., 2004. 40Ar/39Ar chronology of
836 late Pliocene and Early Pleistocene geomagnetic and glacial events in southern
837 Argentina. Timescales of the Paleomagnetic Field, Geophys. Monogr. Ser. 145, 175-
838 190.
839 Singer, B.S., Hoffman, K.A., Chauvin, A., Coe, R.S., Pringle, M.S., 1999. Dating
840 transitionally magnetized lavas of the late Matuyama Chron: Toward a new
841 40Ar/39Ar timescale of reversals and events. J. Geophys. Res. 104, 679-693.

842 Stoner, J.S., Laj, C., Channell, J.E.T., Kissel, C., 2002. South Atlantic and North Atlantic
843 geomagnetic paleointensity stacks (0-80 ka): implications for inter-hemispheric
844 correlation. Quat. Sci. Rev. 21, 1141-1151.
845 Tauxe, L., Labrecque, J., Dodso, D., Fuller, M., 1983. "U" channels - a new technique for
846 paleomagnetic analysis of hydraulic piston cores. Eos, Trans. Amer. Geophys. Union
847 64, 219.
848 Tauxe, L., 1993. Sedimentary records of relative paleointensity of the geomagnetic field:
849 theory and practice. Rev. Geophys. 31, 319-354.
850 Thomas, R.G., Guyodo, Y., Channell, J.E.T., 2003. U channel track for susceptibility
851 measurements. Geochem. Geophys. Geosyst. 4, 1050, doi:10.1029/2002GC000454.
852 Thouveny, N., Bourlès, D.L., Saracco, G., Carcaillet, J.T., Bassinot, F., 2008.
853 Paleoclimatic context of geomagnetic dipole lows and excursions in the Brunhes,
854 clue for an orbital influence on the geodynamo? Earth Planet. Sci. Lett. 275, 269-
855 284.
856 Thouveny, N., Carcaillet, J., Moreno, E., Leduc, G., Nerini, D., 2004. Geomagnetic
857 moment variation and paleomagnetic excursions since 400 kyr BP; a stacked record
858 from sedimentary sequences of the Portuguese margin. Earth Planet. Sci. Lett. 219,
859 377-396.
860 Torrence, C., Compo, G.P., 1998. A practical guide to wavelet analysis. Bull. Am.
861 Meteorol. Soc. 79, 61-78.
862 Torrence, C., Webster, P.J., 1999. Interdecadal changes in the ENSO-monsoon system. J.
863 Climate 12, 2679-2690.

Valet, J.P., Meynadier, L., Guyodo, Y., 2005. Geomagnetic dipole strength and reversal rate over the past two million years. Nature 435, 802-805.

Wang, D.J., Wang, Y.C., Han, J.T., Duan, M.G., Shan, J.Z., Liu, T.S., 2010. Geomagnetic anom- alies recorded in L9 of the Songjiadian loess section in southeastern Chinese Loess Plateau. Chin. Sci. Bull. 55, 520–529.

Weeks, R., Laj, C., Endignoux, L., Fuller, M., Roberts, A., Manganne, R., Blanchard, E., Goree, W., 1993. Improvements in long-core measurement techniques - applications in paleomagnetism and paleoceanography. Geophys. J. Int. 114, 651-662.

Xuan, C., Channell, J.E.T., 2008. Origin of orbital periods in the sedimentary relative paleointensity records. Phys. Earth Planet. Inter. 169, 140-151.

Xuan, C., Channell, J.E.T., 2009. UPmag: MATLAB software for viewing and processing u channel or other pass-through paleomagnetic data. Geochem. Geophys. Geosyst. 10, Q10Y07, Q10Y07, doi:10.1029/2009GC002584.

Xuan, C., Oda, H., 2015. UDECON: deconvolution optimization software for restoring high-resolution records from pass-through paleomagnetic measurements. Earth, Planets Space 67, 183, doi:10.1186/s40623-015-0332-x.

Yamazaki, T., 1999. Relative paleointensity of the geomagnetic field during Brunhes Chron recorded in North Pacific deep-sea sediment cores: orbital influence? Earth Planet. Sci. Lett. 169, 23-35.

Yamazaki, T., Oda, H., 2002. Orbital influence on Earth's magnetic field; 100,000-year periodicity in inclination. Science 295, 2435-2438.

885 Yang, T., Hyodo, M., Yang, Z., Fu, J., 2004. Evidence for the Kamikatsura and Santa
886 Rosa excursions recorded in eolian deposits from the southern Chinese Loess
887 Plateau. J. Geophys. Res. 109, B12105, doi:10.1029/2004JB002966.
888
889
890 **Figure Caption**
891
892 **Figure 1.** Location of IODP Sites U1304 (this study), U1306, and U1308, Core EW9303-
893 17 studied by Bodén and Backman (1996), and ODP Sites 983 and 984. Site U1304 and
894 Core KN166-14-JPC-13 are at the same location. Dashed orange and blue lines depict
895 major surface and deep currents, respectively, in the North Atlantic Ocean. The Subarctic
896 Convergence (Ruddiman and Glover, 1975) is marked by a thick dashed black line.
897 DSOW = Denmark Strait Overflow Water; ISOW = Iceland-Scotland Overflow Water;
898 NAC = North Atlantic Current; CGFZ = Charlie Gibbs Fracture Zone.
899
900 **Figure 2.** (a) Site U1304 depth versus age and resulting sedimentation rates (gray lines).
901 Age models were developed by a combination of correlating Site U1304 volume
902 magnetic susceptibility to that of Core KN166-14-JPC-13 (green triangles), correlating
903 Site U1304 benthic $\delta^{18}O$ to LR04 stack (red circles), and automated matching of Site
904 U1304 RPI to the PISO-1500 RPI stack (blue symbols). Depth-age ties are listed in Table
905 1. (b) Correlation of Site U1304 volume magnetic susceptibility (in blue) to that of Core
906 KN166-14-JPC-13 (red), and (c) the resulting comparison of Site U1304 (blue) and Core

907 KN166-14-JPC-13 (red) RPI proxies. The two RPI records were normalized by their
908 respective mean values for comparison.
909
910 **Figure 3.** (a) Cores from Site U1304 that were sampled using u-channels for this study.
911 (b) Site U1304 benthic $\delta^{18}O$ (blue) with marine isotope stages labeled by dark red
912 numbering. (c) ChRM declination before (light blue) and after correction (green) by
913 uniform rotation of individual cores so that the mean of corrected declinations is oriented
914 north or south for intervals with positive and negative inclinations, respectively. (d)
915 ChRM inclinations (red) with polarity chrons/subchrons and excursions labeled in black.
916 (e) Maximum angular deviation (MAD; black) associated with the ChRM calculation. In
917 (d): E-I, II, and III = Magnetic excursion I, II, and III, Cobb Mtn = Cobb Mountain
918 Subchron. Vertical dark and light gray bars indicate intervals with predominant and
919 disseminated diatom mats (i.e. DRV = 1 or 0.5, see text), and vertical yellow bar denotes
920 a ~3.5-m long interval dominated by a thick diatom mat and that was not sampled.
921
922 **Figure 4.** Orthogonal projections of NRM demagnetization data for representative
923 samples from non-diatom (clay-rich) intervals and diatom-rich intervals (DRV = 0.5 or 1,
924 see text), and for samples from the three recorded magnetic excursion intervals. Circles
925 (red) and squares (blue) indicate projections onto vertical and horizontal planes,
926 respectively (intensity units are mA/m). The peak AFs are 0 (no demagnetization), 20-60
927 mT in 5 mT increments, 60-80 mT in 10 mT intervals, and 100 mT. The 20 mT and/or 80
928 mT demagnetization steps are labeled.
929

930 **Figure 5.** Site U1304: (a) Digital image of the composite splice. (b) Percentage of core
931 section composed of diatom ooze (black, Expedition 303 Scientists, 2006) and relative
932 abundance of *Thalassiothrix longissima* (purple, Shimada et al., 2008). (c) Volume
933 magnetic susceptibility (red). (d) ARM intensity after 35 mT AF demagnetization (blue).
934 (e) IRM intensity after 35 mT AF demagnetization (green). (f) S-ratios (light blue).
935 Vertical dark and light gray bars indicate intervals with predominant and disseminated
936 diatom mats (i.e. DRV = 1 or 0.5, see text), and the vertical yellow bar denotes a ~3.5-m
937 interval dominated by a thick diatom mat that was not sampled.
938
939 **Figure 6.** (a) Hysteresis ratios for Site U1304 samples from each u-channel sample on a
940 Day et al. (1977) plot; and representative hysteresis loops (blue curves) and back field
941 measurements (red curve) from non-diatom (clay-rich) intervals (b and c) and diatom-
942 rich (d and e) sediments. Plotted hysteresis ratios are coloured according to average
943 susceptibility of the u-channel, from which the bulk sediment samples were collected. SD
944 = single domain; PSD = pseudo-single domain; MD = multi-domain.
945
946 **Figure 7.** Comparison of non-diatom (blue) and diatom-rich (red) samples in histograms
947 of: (a) NRM intensity after 35-mT peak field demagnetization, (b) corrected ChRM
948 declinations, (c) ChRM inclinations, (e) ARM intensity after 35-mT peak field
949 demagnetization, and (f) slopes of NRM versus ARM acquisition (RPI proxy). (d)
950 Comparison of linear correlation coefficients (r-values) associated with best-fit lines for
951 NRM lost versus ARM lost (blue), NRM lost versus IRM lost (red), and NRM lost versus

952 ARM acquired (green). Note that NRM and ARM acquisition intensity data in (a) and (e)
953 are on logarithmic scales.
954
955 **Figure 8.** Relative paleointensity (RPI) slope values (bottom panel) and accompanying
956 linear correlation coefficients (r-values, upper panel) for best-fit lines of NRM lost versus
957 ARM lost data (blue) and for NRM lost versus ARM acquired data (red). Slopes were
958 determined using NRM and ARM data from the 20-60 mT demagnetization/acquisition
959 interval, at 1-cm intervals. Vertical dark and light gray bars indicate intervals with
960 predominant and disseminated diatom mats (i.e. DRV = 1 or 0.5, see text), and the
961 vertical yellow bar denotes a ~3.5-m interval dominated by a thick diatom mat that was
962 not sampled.
963
964 **Figure 9.** Site U1304: (a) ARM intensity after 35 mT demagnetization (green), (b)
965 benthic $\delta^{18}O$ (red) compared with the LR04 stack (blue, Lisiecki and Raymo, 2005), (c)
966 sedimentation rate (black), (d) interpretation of magnetic polarity stratigraphy, (e) ChRM
967 inclination, and (f) RPI (red) compared with the PISO-1500 RPI stack (blue). Light blue
968 labels in (b) mark marine isotope stages. In (d): E-I, II, and III = Magnetic excursions I,
969 II, and III, Ja. = Jaramillo Subchron, and Cobb Mtn = Cobb Mountain Subchron. Site
970 U1304 and PISO-1500 RPI records were normalized by their mean values for comparison
971 in (f). Vertical dark and light gray bars indicate intervals with predominant and
972 disseminated diatom mats (i.e. DRV = 1 or 0.5, see text), and the vertical yellow bar
973 denotes a ~3.5-m interval dominated by a thick diatom mat that was not sampled.
974

975 **Figure 10.** (a) IODP Site U1304 RPI record (red) compared with RPI records from ODP
976 Sites 983 (blue) and 984 (light blue) (Channell et al., 1997, 2002; Channell, 1999,
977 Channell and Kleiven, 2000), and from IODP Site U1306 (gray) (Channell et al., 2014).
978 (b) The HINAPIS-1500 RPI stack (red) compared with the PISO-1500 RPI stack (black)
979 (Channell et al., 2009) with 90% confidence level estimated through 10,000 bootstrapped
980 populations (gray). (c) Number of RPI values that each RPI record contributes to time
981 intervals in the HINAPIS-1500 stack. Note that all RPI shown in (a) and (b) are
982 normalized by their mean values for the 0-1.5 Ma time interval for comparison.
983
984 **Supplementary Figure 1.** Comparison of ChRM (a) declinations, and (b) inclinations for
985 u-channel sample U1304-18H-3A calculated using PCA of 20-80 mT demagnetization
986 data before (in blue) and after deconvolution (in red). Deconvolution is performed using
987 the UDECON software (Oda and Xuan, 2014; Xuan and Oda, 2015). ChRM directions
988 calculated using deconvolved data clearly show the excursion, suggesting the observed
989 excursion is not caused by the negative-lobe effect associated with the magnetometer
990 sensor response.
991
992 **Supplementary Figure 2.** Magnetic excursion III. U-channel-acquired ChRM (a)
993 inclinations and (b) declinations from Core U1304B-22H (in red) in the 219-222 mcd
994 interval, compared with shipboard data for the same hole (in blue) and from other holes:
995 U1304D-16H (green) and U1304A-22H (black). (c) Shipboard magnetic susceptibility
996 and (d) natural gamma radiation (NGR) data for the three holes during the same interval.
997 Shipboard NRM inclinations of Cores U1304B-22H and U1304D-16H are after 10 mT

998 peak AF demagnetization (the maximum peak field used on the ship for these cores), and
999 shipboard NRM inclinations for Core U1304A-22H are from measurements after 20-mT
1000 peak AF demagnetization. The depths (mcd) of Cores U1304D-16H and U1304A-22H
1001 were adjusted down-section by 5 cm and 20 cm, respectively, relative to core U1304B-
1002 22H for improved correlation of the magnetic susceptibility and NGR data from different
1003 holes. Shipboard declination data for the three cores were corrected to have similar mean
1004 values as the u-channel ChRM declinations of Core U1304B-22H outside the excursion
1005 interval.
1006
1007 **Supplementary Figure 3.** Left column: local wavelet power spectrum (LWPS) for (a)
1008 the Site U1304 RPI record, (b) the HINAPIS-1500 RPI stack, and (c) the PISO-1500 RPI
1009 stack. Middle column: global wavelet power spectrum (GWPS) for (d) the Site U1304
1010 RPI record, (e) the HINAPIS-1500 RPI stack, and (f) the PISO-1500 RPI stack. Right
1011 column: squared wavelet coherence (WTC) between (g) the Site U1304 and the
1012 HINAPIS-1500 RPI data, (h) the PISO-1500 and the HINAPIS-1500 RPI stacks, and (i)
1013 the PISO-1500 and Site U1304 RPI data. Values of normalized wavelet power and
1014 squared wavelet coherence are indicated on LWPS and WTC maps by blue to red colors
1015 for increasing values. The 1% significance level against red noise is shown as thick
1016 (black) contours on LWPS and WTC maps. The cones of influence (COI), where edge
1017 effects make the analyses unreliable, are marked by hachured areas. On the WTC maps,
1018 the relative phase relationship is shown as arrows (in-phase pointing right, anti-phase
1019 pointing left; the arrow points upward where the first signal (i.e. U1304 RPI in (g), PISO-
1020 1500 RPI in (h) and (i)) leads second signal (i.e. HINAPIS-1500 RPI in (g) and (h),

1021 U1304 in (i)) by 90°). Orbital cycles with periods of 400 kyr, 100 kyr, 41 kyr, and 23 kyr

1022 are marked as white dashed lines.

Table 1. Site U1304 age model.

Depth (mcd)	Age (ka)	Method	Depth (mcd)	Age (ka)	Method	Depth (mcd)	Age (ka)	Method	Depth (mcd)	Age (ka)	Method
0.00	0.00	(a)	136.47	739.97	(c)	183.19	1126.25	(d)	206.01	1325.09	(d)
0.96	2.64	(b)	136.85	746.55	(c)	183.41	1129.24	(d)	206.24	1328.08	(d)
3.66	14.79	(b)	140.88	794.63	(c)	183.63	1132.23	(d)	206.46	1329.57	(d)
4.31	17.42	(b)	142.92	822.43	(c)	183.86	1136.72	(d)	206.68	1331.07	(d)
4.75	24.08	(b)	143.40	826.27	(c)	184.08	1141.20	(d)	206.91	1332.56	(d)
5.89	41.01	(b)	145.24	839.44	(c)	184.31	1144.19	(d)	207.13	1334.06	(d)
7.79	55.33	(b)	148.17	864.14	(c)	184.53	1147.18	(d)	207.35	1335.55	(d)
8.10	57.57	(b)	148.87	871.88	(c)	184.75	1148.68	(d)	207.58	1337.05	(d)
8.36	59.42	(b)	149.30	888.55	(c)	185.65	1153.16	(d)	207.80	1340.04	(d)
9.39	68.62	(b)	150.00	900.35	(c)	185.87	1154.66	(d)	208.92	1346.02	(d)
10.75	79.00	(b)	153.79	916.04	(c)	186.32	1159.14	(d)	209.59	1349.01	(d)
11.83	86.32	(b)	158.15	956.00	(c)	186.54	1162.13	(d)	210.04	1350.50	(d)
12.91	93.48	(b)	158.50	964.19	(c)	186.99	1169.61	(d)	210.71	1352.00	(d)
13.60	98.94	(b)	162.39	978.80	(c)	187.21	1174.09	(d)	211.38	1353.49	(d)
14.39	104.05	(b)	164.00	990.00	(c)	187.44	1178.58	(d)	211.83	1354.99	(d)
14.87	107.53	(b)	165.91	997.99	(c)	187.66	1183.06	(d)	212.05	1356.48	(d)
15.02	108.25	(b)	166.18	1012.63	(d)	187.89	1187.55	(d)	212.50	1360.97	(d)
15.77	110.34	(b)	166.40	1017.12	(d)	188.11	1192.03	(d)	212.95	1368.44	(d)
19.98	119.86	(b)	166.63	1021.60	(d)	188.33	1196.52	(d)	213.17	1371.43	(d)
21.94	123.70	(b)	166.85	1026.09	(d)	188.56	1201.00	(d)	213.40	1372.93	(d)
22.39	126.07	(c)	167.08	1029.08	(d)	188.78	1205.49	(d)	213.84	1374.42	(d)
22.66	134.81	(c)	167.30	1030.57	(d)	189.00	1209.97	(d)	214.51	1375.92	(d)
25.35	188.37	(c)	167.97	1033.56	(d)	189.23	1211.47	(d)	215.63	1378.91	(d)
27.83	204.19	(c)	169.09	1038.05	(d)	189.68	1212.96	(d)	216.08	1380.40	(d)
31.02	216.90	(c)	170.21	1042.53	(d)	190.80	1215.95	(d)	216.30	1381.90	(d)
31.42	223.31	(c)	171.33	1047.02	(d)	191.24	1217.45	(d)	216.53	1384.89	(d)
32.14	229.88	(c)	171.77	1048.51	(d)	191.91	1220.44	(d)	216.75	1389.37	(d)
34.30	240.03	(c)	172.89	1051.50	(d)	192.14	1221.93	(d)	217.20	1396.85	(d)
34.90	245.76	(c)	173.56	1053.00	(d)	192.36	1223.43	(d)	217.87	1402.83	(d)
38.25	277.28	(c)	174.24	1054.49	(d)	192.59	1224.92	(d)	218.09	1405.82	(d)
40.70	293.24	(c)	174.91	1055.99	(d)	193.48	1232.40	(d)	218.32	1410.30	(d)
41.45	299.26	(c)	175.13	1057.48	(d)	194.15	1238.38	(d)	218.54	1414.79	(d)
42.77	305.15	(c)	175.35	1060.47	(d)	194.60	1242.86	(d)	218.77	1419.27	(d)
51.58	332.01	(c)	175.58	1063.46	(d)	195.05	1250.34	(d)	218.99	1423.76	(d)
52.24	341.35	(c)	175.80	1066.45	(d)	195.27	1254.82	(d)	219.21	1428.24	(d)
54.09	374.47	(c)	176.03	1070.94	(d)	195.49	1259.31	(d)	219.44	1432.73	(d)
59.84	391.82	(c)	176.25	1073.93	(d)	195.72	1262.30	(d)	219.66	1437.21	(d)
71.78	423.34	(c)	176.47	1075.42	(d)	196.17	1266.78	(d)	219.89	1441.70	(d)
72.38	432.03	(c)	177.37	1079.91	(d)	197.06	1274.26	(d)	220.11	1446.18	(d)
74.85	474.92	(c)	177.59	1081.40	(d)	197.96	1281.73	(d)	220.33	1450.67	(d)
75.54	483.92	(c)	177.82	1085.89	(d)	198.18	1283.23	(d)	220.56	1455.15	(d)
100.87	530.75	(c)	178.04	1090.37	(d)	198.40	1284.72	(d)	220.78	1459.64	(d)
103.99	552.39	(c)	178.49	1094.86	(d)	199.30	1289.21	(d)	221.00	1464.12	(d)
110.97	577.36	(c)	178.71	1096.35	(d)	199.97	1292.20	(d)	221.23	1468.61	(d)
112.57	584.97	(c)	178.94	1097.85	(d)	201.09	1296.68	(d)	221.45	1473.09	(d)
119.78	613.56	(c)	179.38	1102.33	(d)	202.21	1299.67	(d)	221.68	1477.58	(d)
121.47	629.71	(c)	179.83	1106.82	(d)	203.33	1302.66	(d)	221.90	1482.06	(d)
123.64	662.50	(c)	180.05	1108.31	(d)	204.44	1305.65	(d)	222.12	1486.55	(d)
125.12	685.03	(c)	180.73	1111.30	(d)	204.89	1307.15	(d)	222.35	1491.03	(d)
125.61	690.30	(c)	181.84	1115.79	(d)	205.12	1308.64	(d)	222.57	1495.52	(d)
130.51	709.99	(c)	182.52	1118.78	(d)	205.34	1311.63	(d)	222.79	1500.00	(d)
131.20	717.38	(c)	182.74	1120.27	(d)	205.56	1316.12	(d)	262.00	1778.00	(e)
132.91	728.04	(c)	182.96	1123.26	(d)	205.79	1320.60	(d)			

Method (a) = core top has present age; (b) = correlation of U1304 susceptibility to that of core KN166-14-JPC-13 (Hodell et al., 2010); (c) = correlation of U1304 benthic $\delta^{18}O$ to LR04 stack (Lisiecki and Raymo, 2005); (d) = automated matching (Lisiecki and Lisiecki, 2002) of Site U1304 RPI to the PISO-1500 RPI stack (Channell et al., 2009); and (e) top of the Olduvai subchron according to shipboard paleomagnetic data (Expedition 303 Scientists, 2006).

Table 2. Geomagnetic reversals and excursions recorded at Site U1304.

Reversal/Excursions	Top		Bottom		Center		
	Depth (mcd)	Age (ka)	Depth (mcd)	Age (ka)	Depth (mcd)	Age (ka)	MIS
(b) C1n (M/B Boundary)	138.59	767.31	139.36	776.50	138.98	771.96	19
(t) C1r.1n (Jaramillo)	164.43	991.80	164.82	993.43	164.63	992.64	28
(b) C1r.1n (Jaramillo)	175.96	1069.62	176.11	1072.07	176.04	1071.13	31
(t) C1r.2n (Cobb Mountain)	188.14	1192.65	188.2	1193.85	188.17	1193.25	35
(b) C1r.2n (Cobb Mountain)	191.38	1218.06	191.7	1219.49	191.54	1218.78	37
Magnetic Excursion I	149.23	885.84	149.34	889.22	149.29	887.97	22/23
Magnetic Excursion II	182.96	1123.22	183.02	1124.02	182.99	1123.62	34
Magnetic Excursion III	220.75	1459.04	221.18	1467.67	220.97	1463.46	48/49

(b) = base; (t) = top.; M/B = Matuyama/Brunhes; MIS = Marine Isotope Stage. Estimated ages are based on linear interpolation of age model in Table 1.

Figure 1.

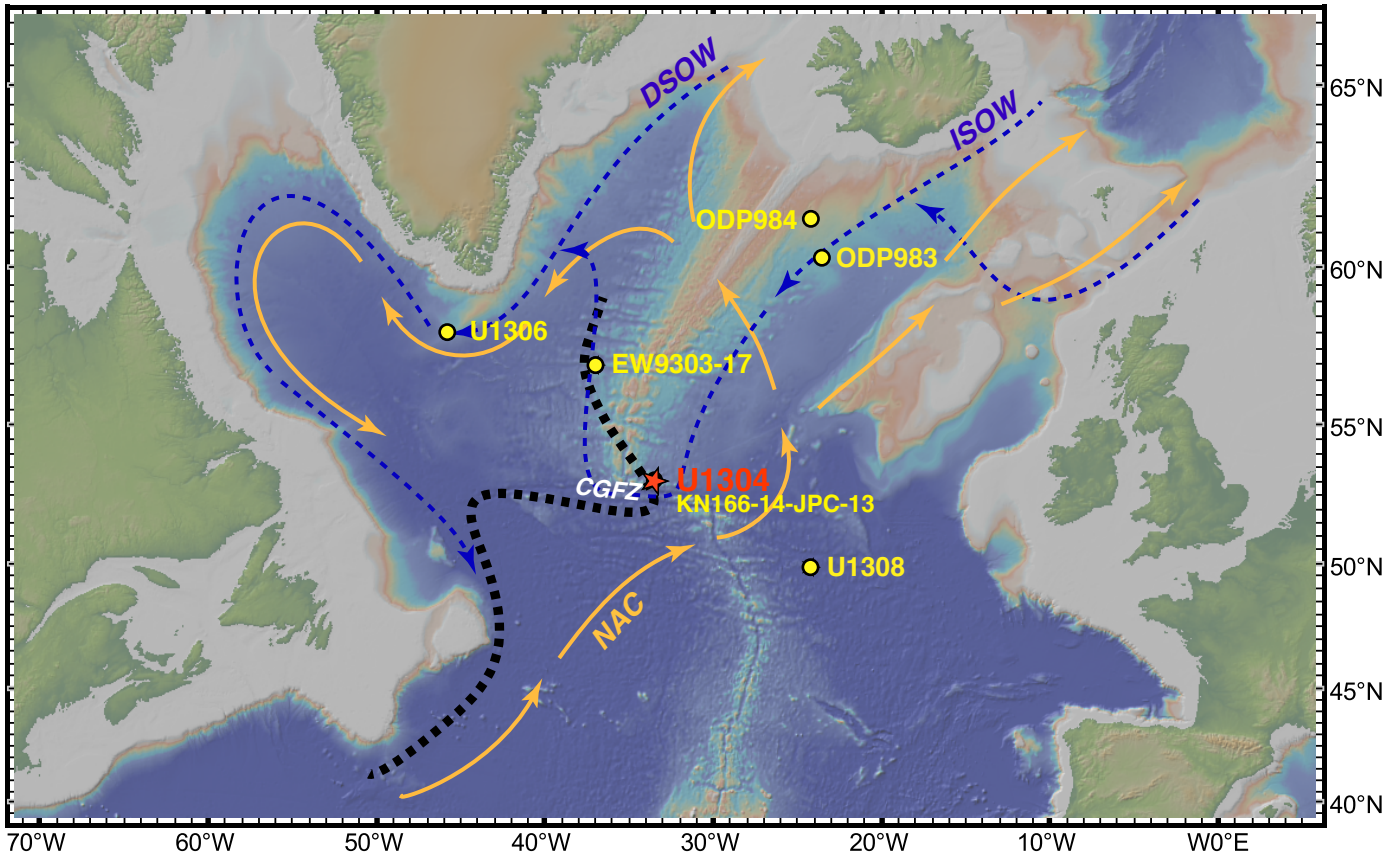
DSOW
ISOW
ODP984
ODP983
U1306
EW9303-17
CGFZ
U1304
KN166-14-JPC-13
U1308
NAC
65°N
60°N
55°N
50°N
45°N
40°N
70°W
60°W
50°W
40°W
30°W
20°W
10°W
W0°E

Figure 2.

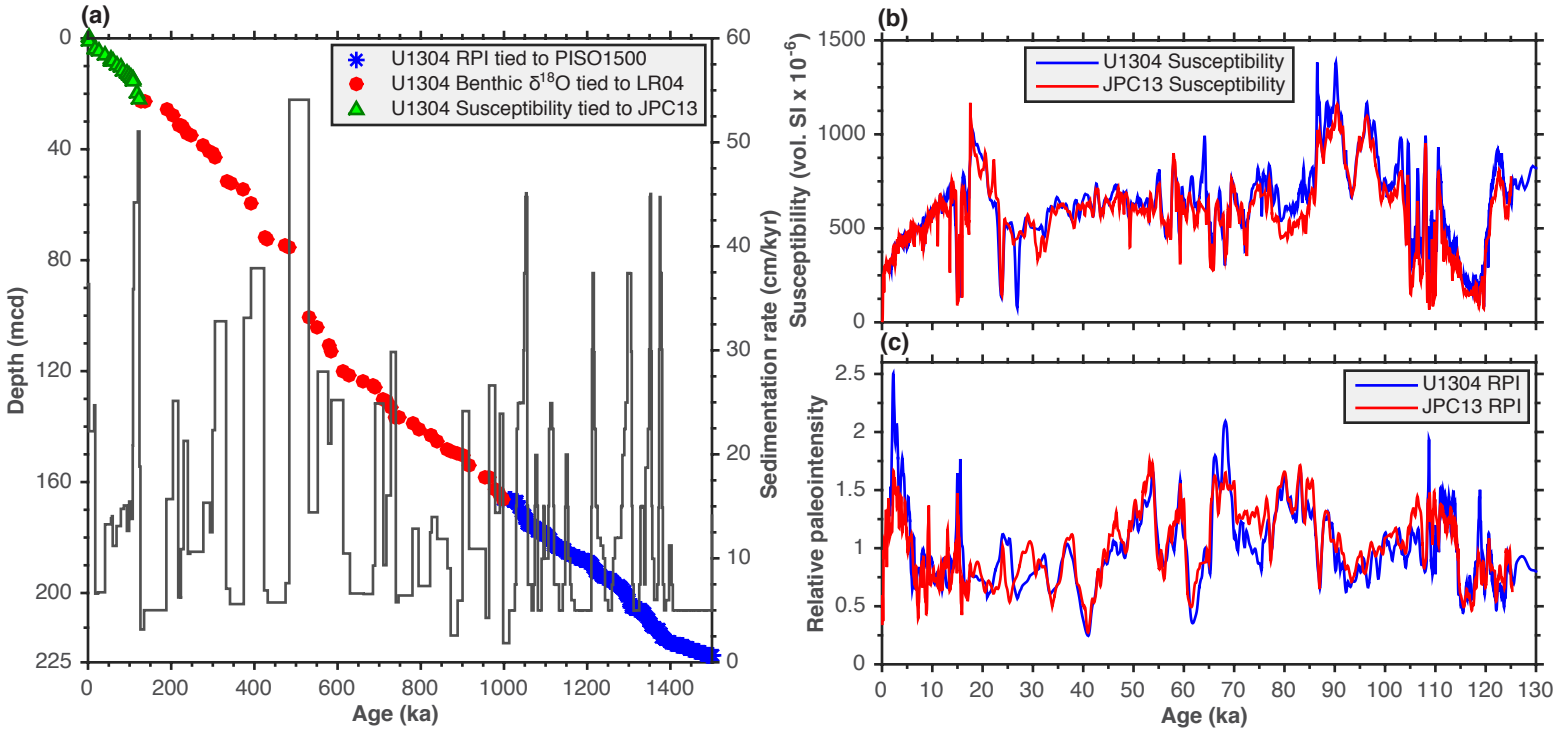
(a)
U1304 RPI tied to PISO1500
U1304 Benthic δ18O tied to LR04
U1304 Susceptibility tied to JPC13
Depth (mcd)
Sedimentation rate (cm/kyr)
Age (ka)
(b)
U1304 Susceptibility
JPC13 Susceptibility
Susceptibility (vol. SI x 10-6)
(c)
U1304 RPI
JPC13 RPI
Relative paleointensity
Age (ka)

Figure 3.

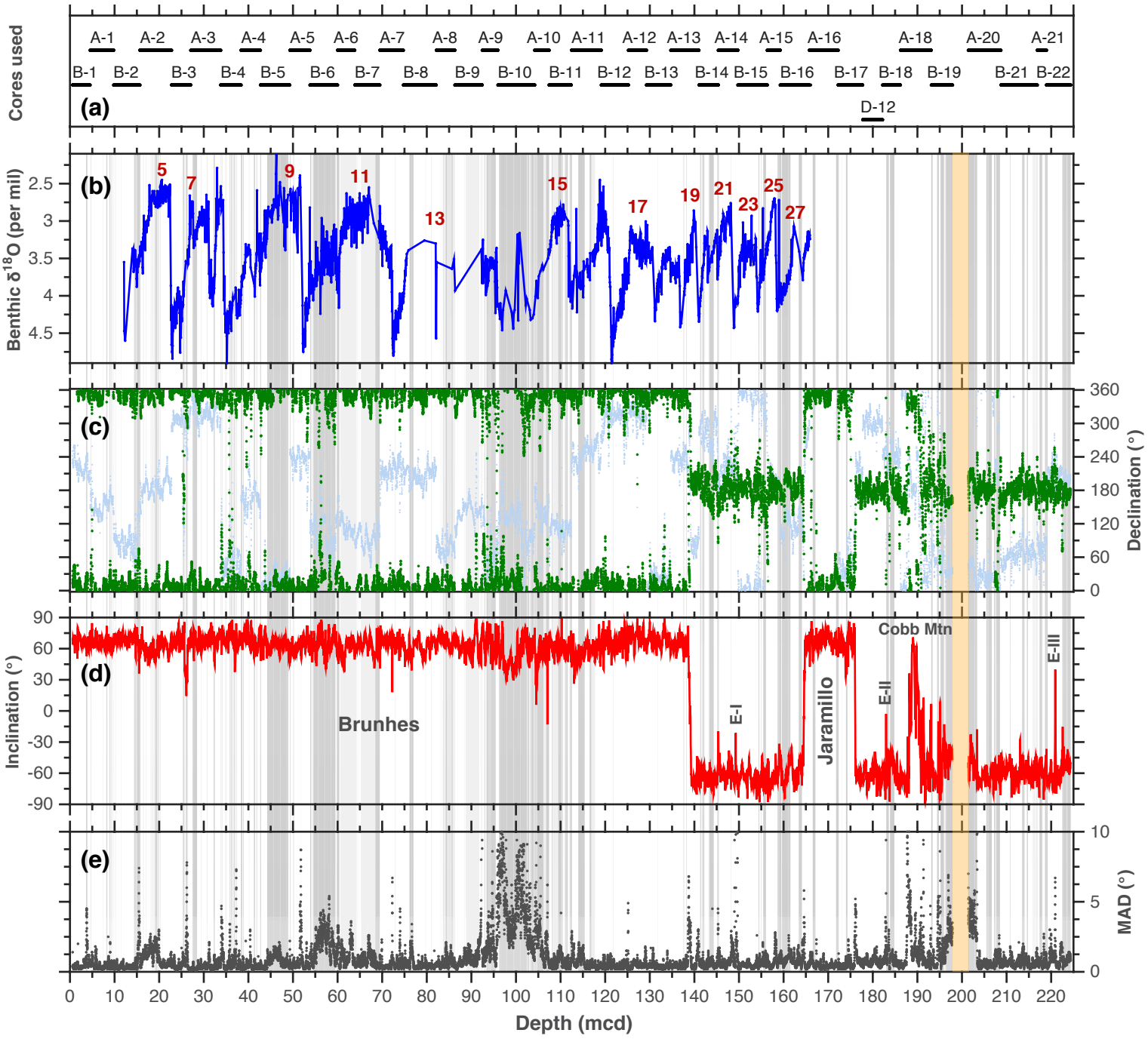
Cores used
A-1 A-2 A-3 A-4 A-5 A-6 A-7 A-8 A-9 A-10 A-11 A-12 A-13 A-14 A-15 A-16 A-18 A-20 A-21
B-1 B-2 B-3 B-4 B-5 B-6 B-7 B-8 B-9 B-10 B-11 B-12 B-13 B-14 B-15 B-16 B-17 B-18 B-19 B-21 B-22
D-12
(a)
(b)
Benthic δ18O (per mil)
2.5
3
3.5
4
4.5
5
7
9
11
13
15
17
19
21
23
25
27
(c)
Declination (°)
360
300
240
180
120
60
0
(d)
Inclination (°)
90
60
30
0
-30
-60
-90
Brunhes
E-I
Jaramillo
E-II
Cobb Mtn
E-III
(e)
MAD (°)
10
5
0
0 10 20 30 40 50 60 70 80 90 100 110 120 130 140 150 160 170 180 190 200 210 220
Depth (mcd)

Figure 4.

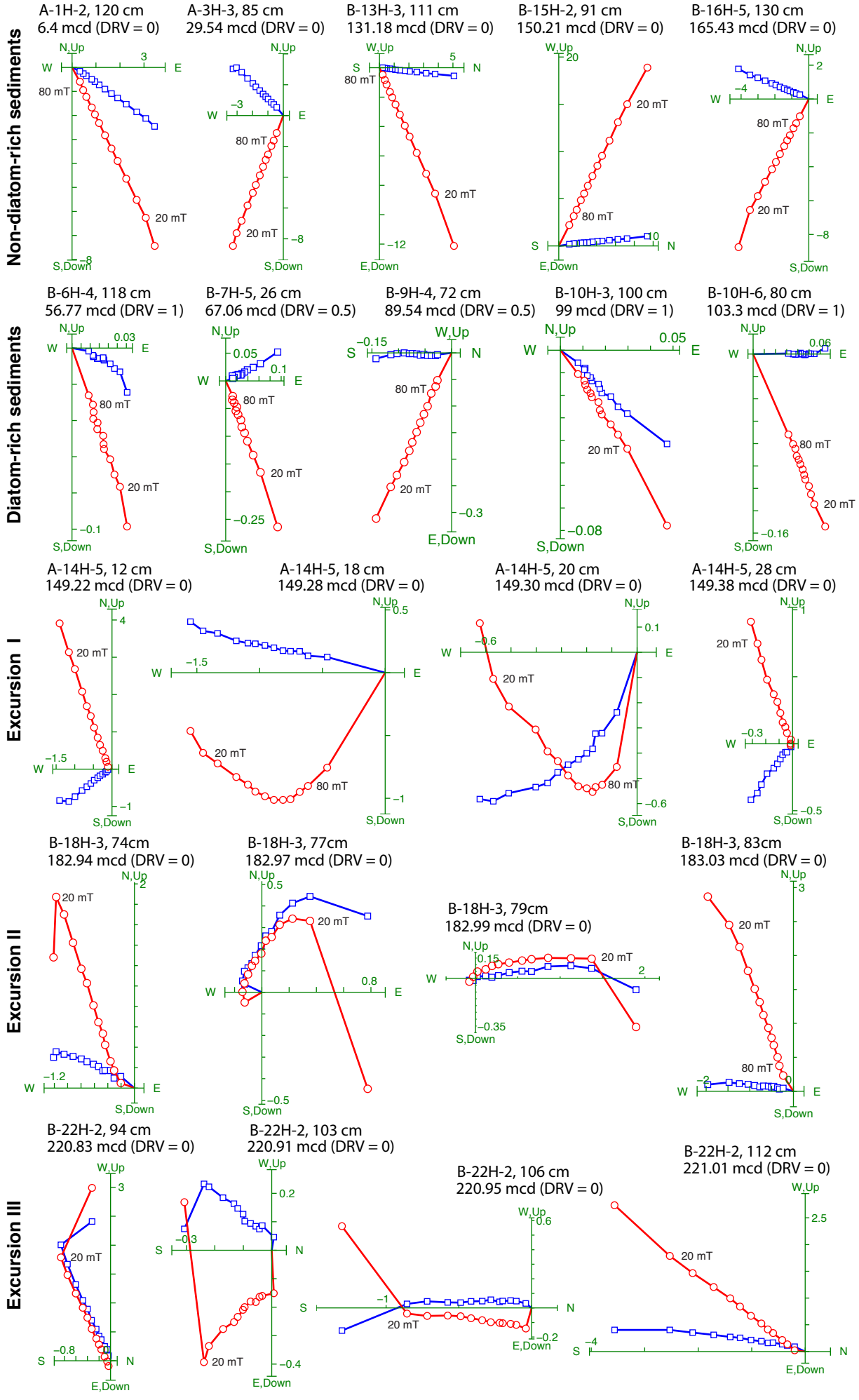
Non-diatom-rich sediments
A-1H-2, 120 cm
6.4 mcd (DRV = 0)
A-3H-3, 85 cm
29.54 mcd (DRV = 0)
B-13H-3, 111 cm
131.18 mcd (DRV = 0)
B-15H-2, 91 cm
150.21 mcd (DRV = 0)
B-16H-5, 130 cm
165.43 mcd (DRV = 0)
Diatom-rich sediments
B-6H-4, 118 cm
56.77 mcd (DRV = 1)
B-7H-5, 26 cm
67.06 mcd (DRV = 0.5)
B-9H-4, 72 cm
89.54 mcd (DRV = 0.5)
B-10H-3, 100 cm
99 mcd (DRV = 1)
B-10H-6, 80 cm
103.3 mcd (DRV = 1)
Excursion I
A-14H-5, 12 cm
149.22 mcd (DRV = 0)
A-14H-5, 18 cm
149.28 mcd (DRV = 0)
A-14H-5, 20 cm
149.30 mcd (DRV = 0)
A-14H-5, 28 cm
149.38 mcd (DRV = 0)
Excursion II
B-18H-3, 74cm
182.94 mcd (DRV = 0)
B-18H-3, 77cm
182.97 mcd (DRV = 0)
B-18H-3, 79cm
182.99 mcd (DRV = 0)
B-18H-3, 83cm
183.03 mcd (DRV = 0)
Excursion III
B-22H-2, 94 cm
220.83 mcd (DRV = 0)
B-22H-2, 103 cm
220.91 mcd (DRV = 0)
B-22H-2, 106 cm
220.95 mcd (DRV = 0)
B-22H-2, 112 cm
221.01 mcd (DRV = 0)

Figure 5.

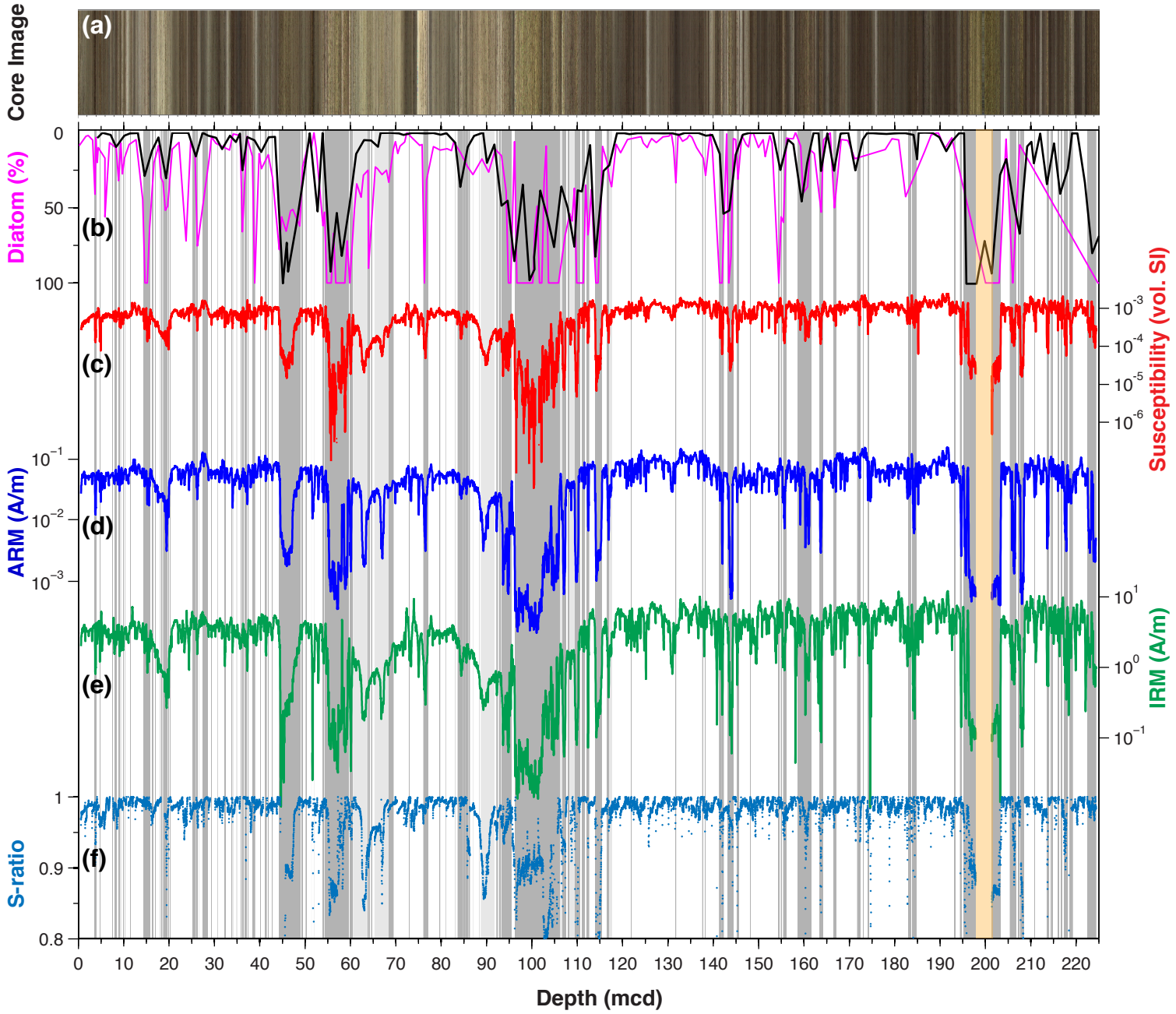
Core Image
(a)
Diatom (%)
0
50
100
(b)
(c)
Susceptibility (vol. SI)
10^{-3}
10^{-4}
10^{-5}
10^{-6}
ARM (A/m)
10^{-1}
10^{-2}
10^{-3}
(d)
(e)
IRM (A/m)
10^{1}
10^{0}
10^{-1}
S-ratio
1
0.9
0.8
(f)
0 10 20 30 40 50 60 70 80 90 100 110 120 130 140 150 160 170 180 190 200 210 220
Depth (mcd)

Figure 6.

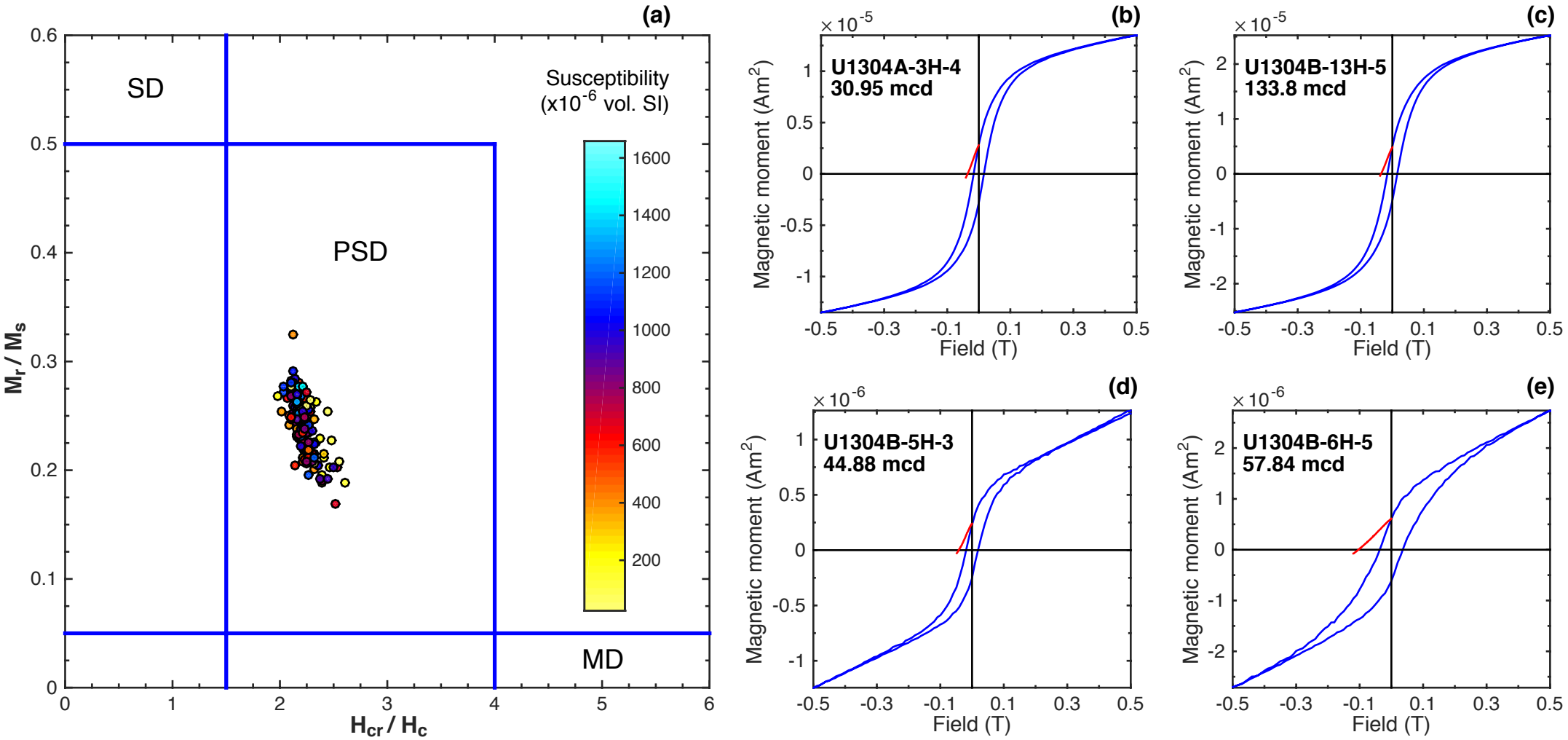
(a)
SD
PSD
MD
Susceptibility
(x10-6 vol. SI)
1600
1400
1200
1000
800
600
400
200
Mr / Ms
Hcr / Hc
(b)
U1304A-3H-4
30.95 mcd
(c)
U1304B-13H-5
133.8 mcd
(d)
U1304B-5H-3
44.88 mcd
(e)
U1304B-6H-5
57.84 mcd
Magnetic moment (Am2)
Field (T)

Figure 7.

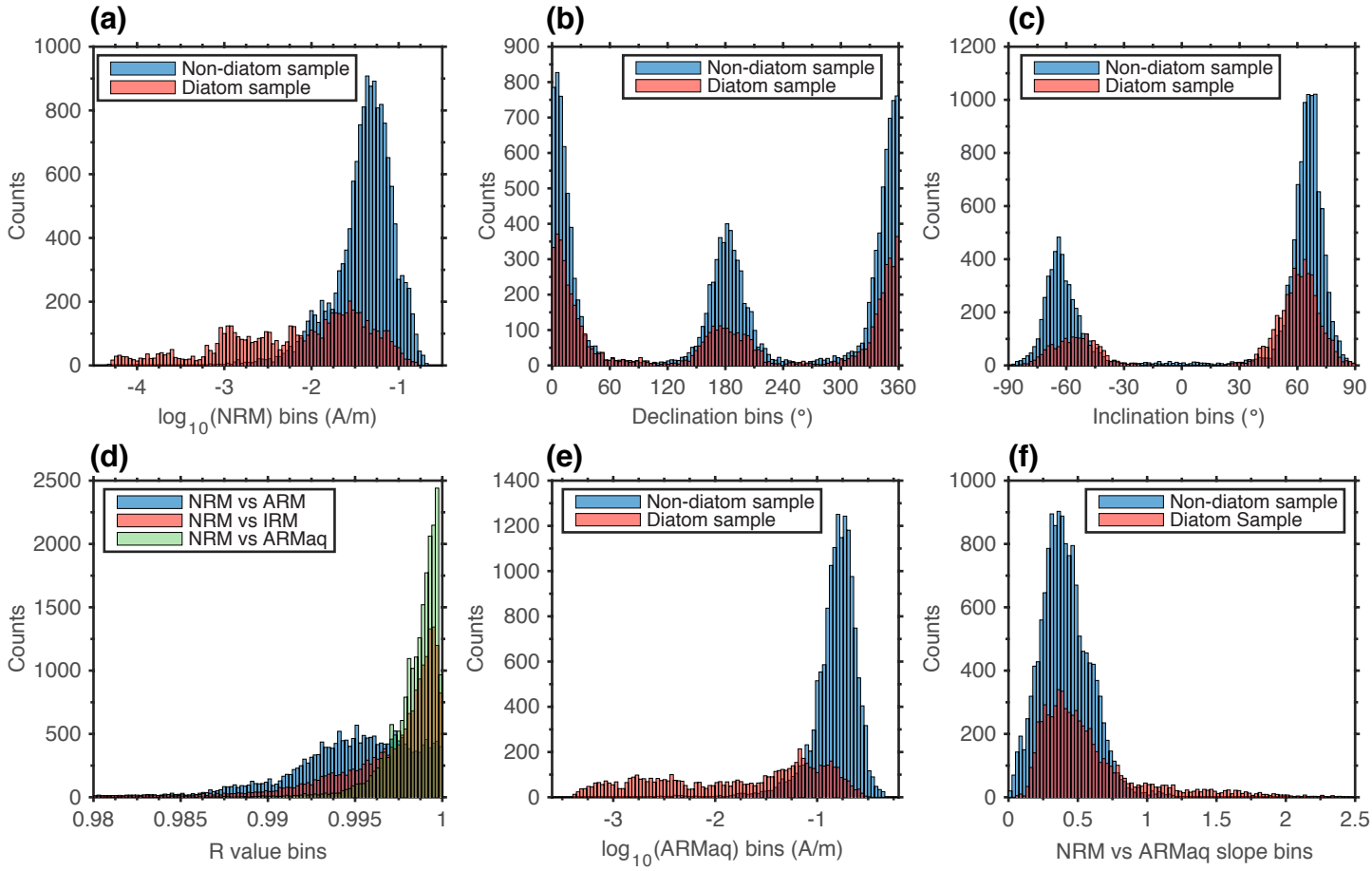
(a)
Non-diatom sample
Diatom sample
Counts
log10(NRM) bins (A/m)
(b)
Non-diatom sample
Diatom sample
Counts
Declination bins (°)
(c)
Non-diatom sample
Diatom sample
Counts
Inclination bins (°)
(d)
NRM vs ARM
NRM vs IRM
NRM vs ARMaq
Counts
R value bins
(e)
Non-diatom sample
Diatom sample
Counts
log10(ARMaq) bins (A/m)
(f)
Non-diatom sample
Diatom Sample
Counts
NRM vs ARMaq slope bins

Figure 8.

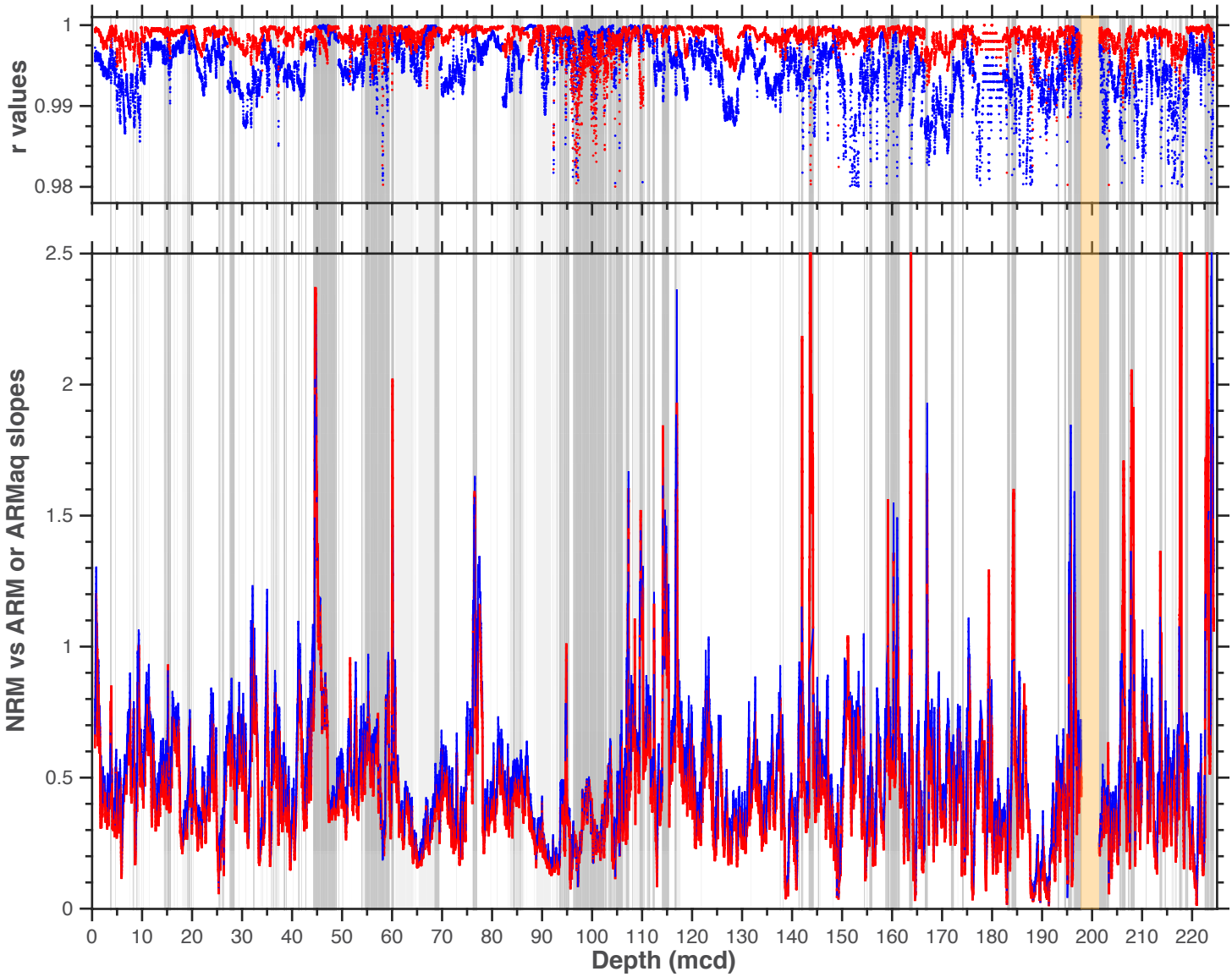
r values
1
0.99
0.98
NRM vs ARM or ARMaq slopes
2.5
2
1.5
1
0.5
0
0
10
20
30
40
50
60
70
80
90
100
110
120
130
140
150
160
170
180
190
200
210
220
Depth (mcd)

Figure 9.

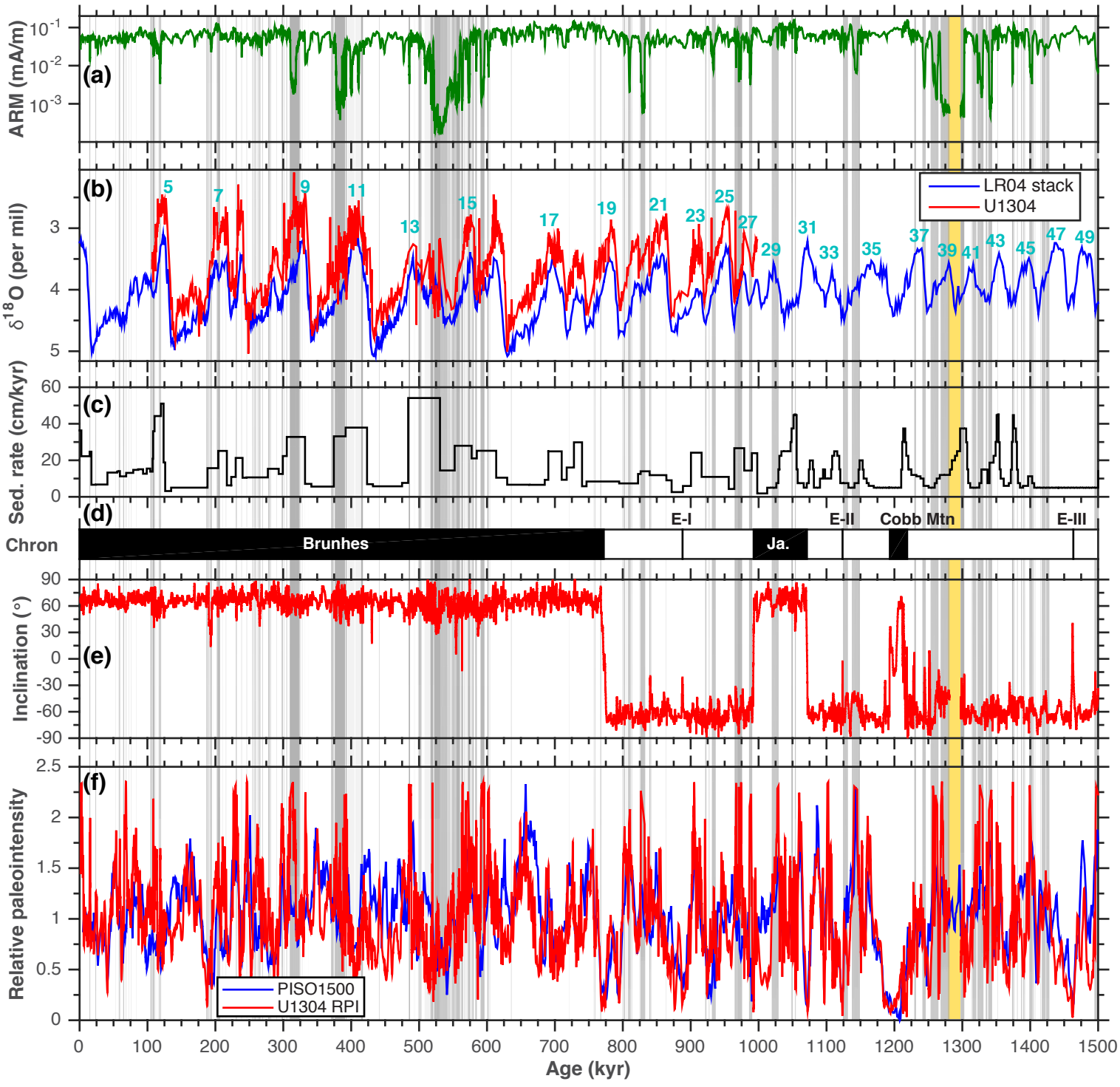
(a)
ARM (mA/m)
10^-1
10^-2
10^-3
(b)
δ18O (per mil)
LR04 stack
U1304
5
7
9
11
13
15
17
19
21
23
25
27
29
31
33
35
37
39
41
43
45
47
49
(c)
Sed. rate (cm/kyr)
(d)
Chron
Brunhes
E-I
Ja.
E-II
Cobb Mtn
E-III
(e)
Inclination (°)
(f)
Relative paleointensity
PISO1500
U1304 RPI
Age (kyr)

Figure 10.

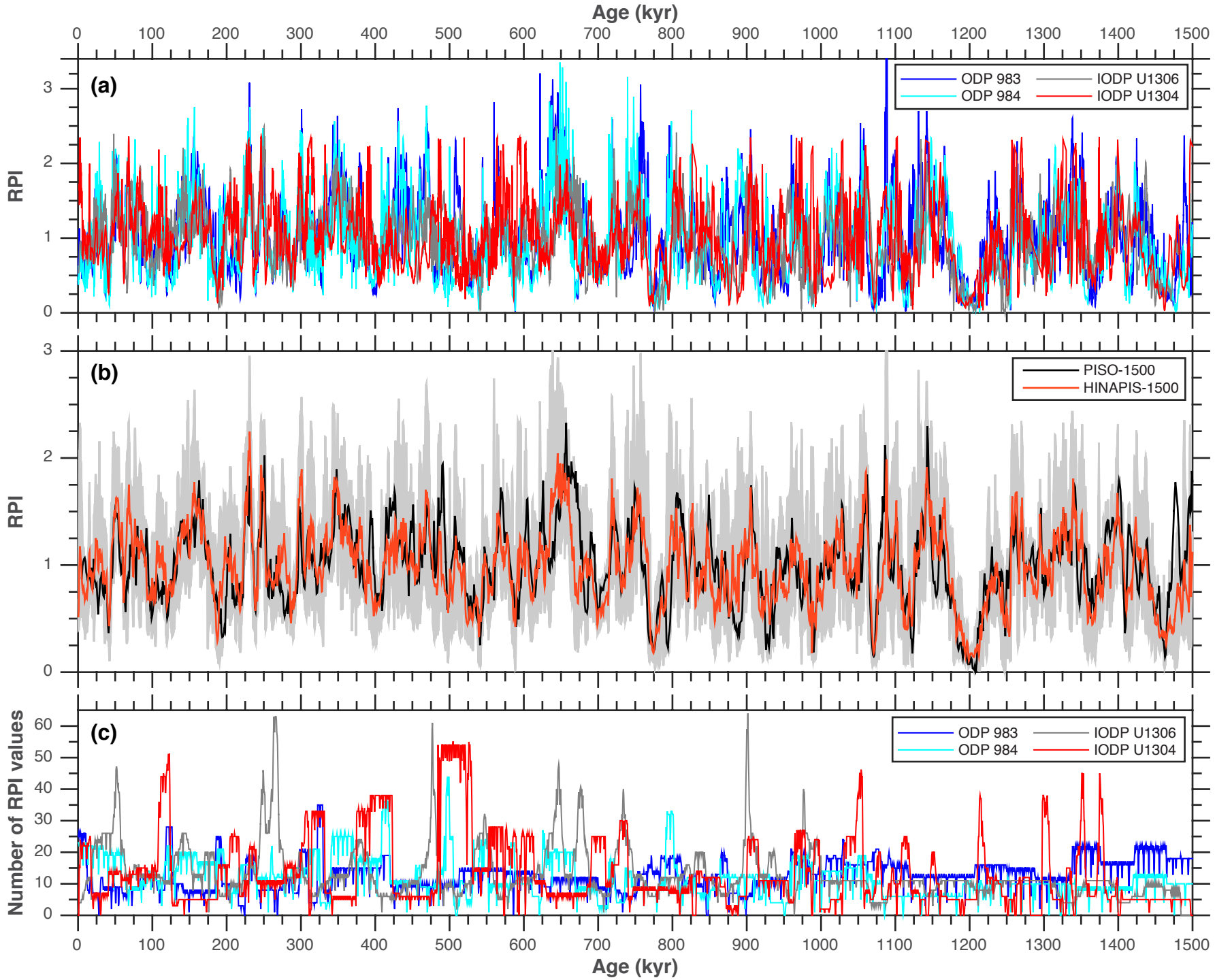
Age (kyr)
(a)
RPI
ODP 983
ODP 984
IODP U1306
IODP U1304
(b)
RPI
PISO-1500
HINAPIS-1500
(c)
Number of RPI values
ODP 983
ODP 984
IODP U1306
IODP U1304
Age (kyr)

Supplementary Figure 1.

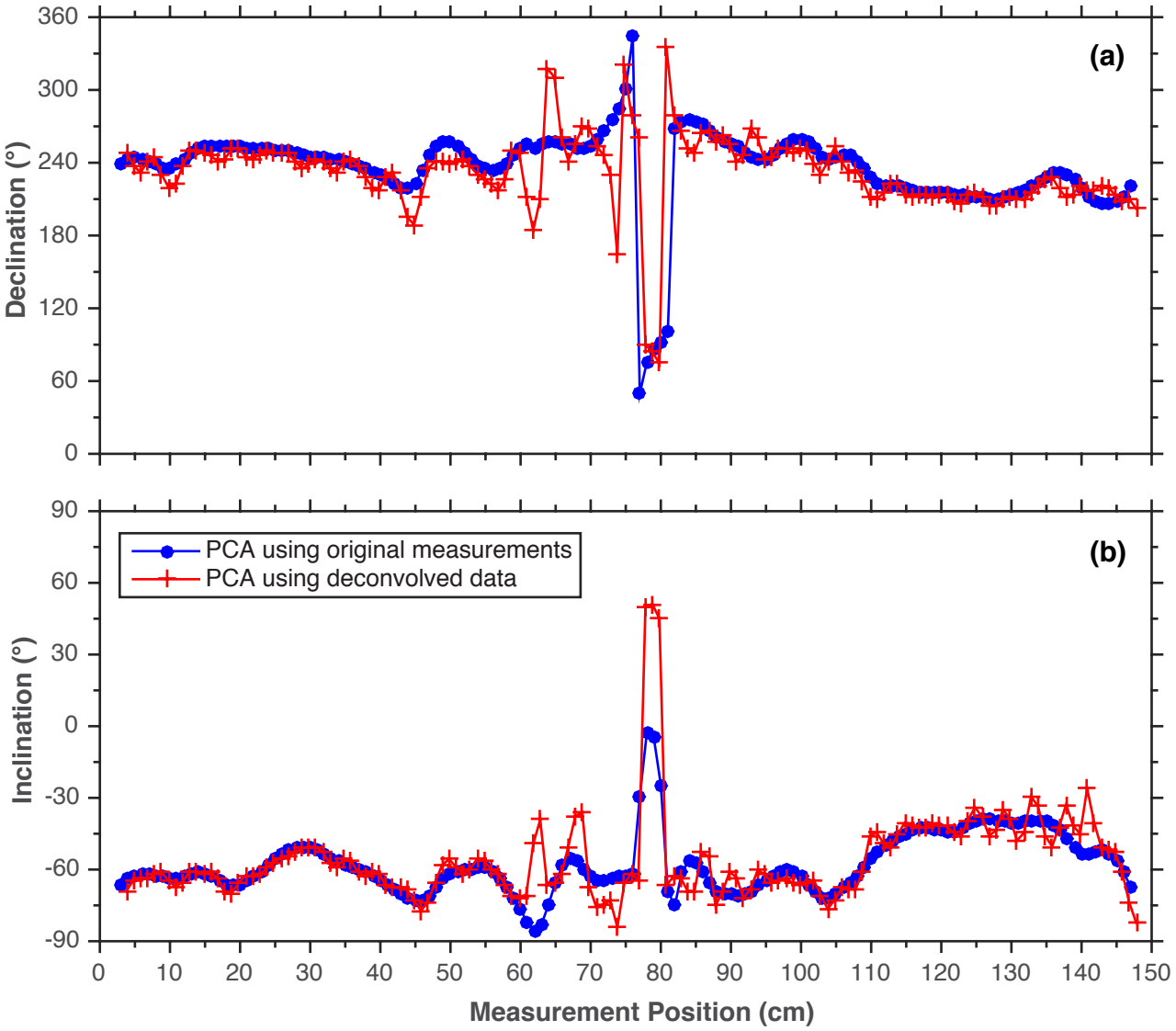

Supplementary Figure 2.

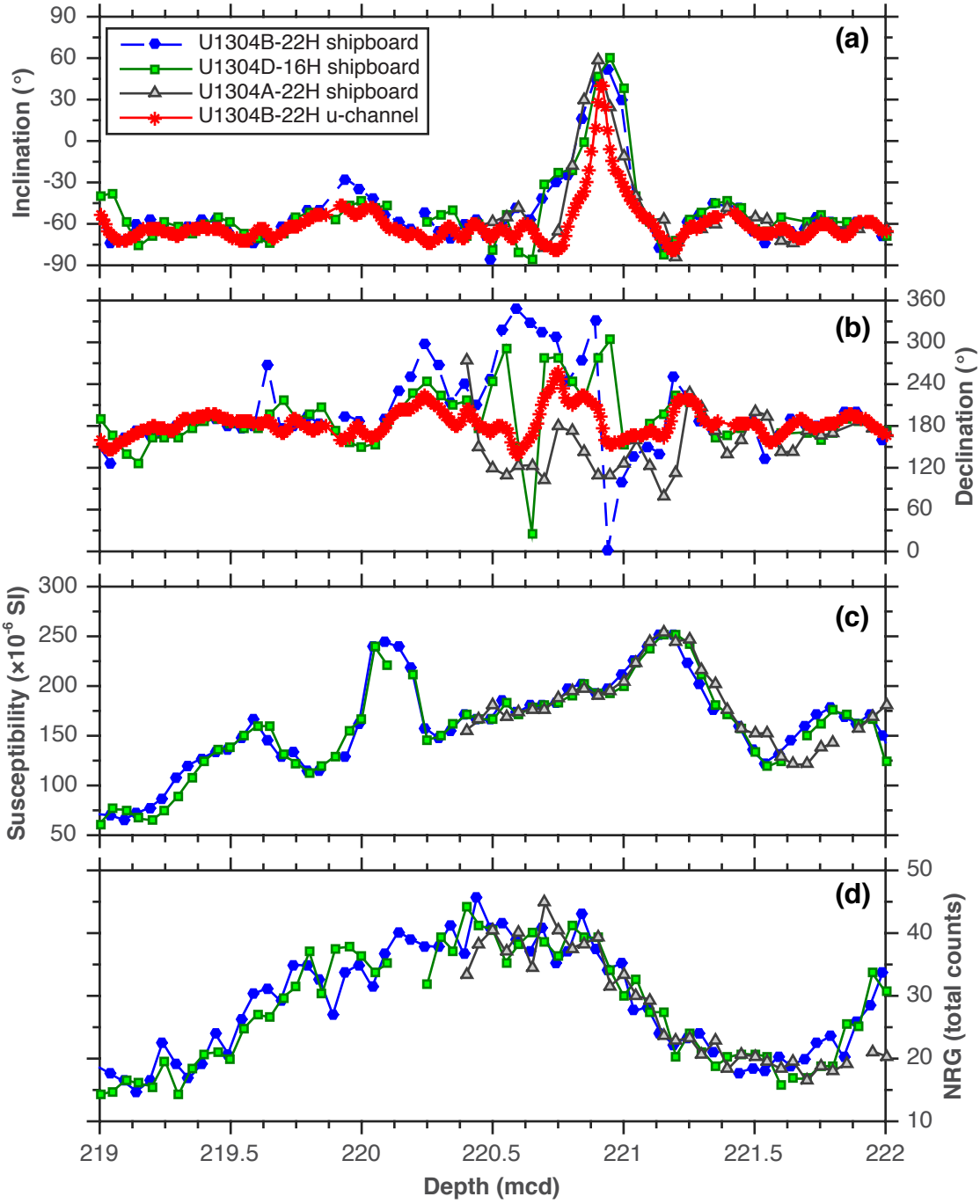

Supplementary Figure 3.